

# The transient event in NGC 1566 from 2017 to 2019

## I. An eccentric accretion disk and a turbulent, disk-dominated broad-line region unveiled by double-peaked Ca II and O I lines<sup>\*</sup>

M.W. Ochmann<sup>1,2</sup>, W. Kollatschny<sup>1</sup>, M.A. Probst<sup>1</sup>, E. Romero-Colmenero<sup>3,4</sup>, D.A.H. Buckley<sup>3,4,5,6</sup>, D. Chelouche<sup>7,8</sup>, R. Chini<sup>2,9,10</sup>, D. Grupe<sup>11</sup>, M. Haas<sup>2</sup>, S. Kaspi<sup>12</sup>, S. Komossa<sup>13</sup>, M.L. Parker<sup>14</sup>, M. Santos-Lleo<sup>15</sup>, N. Schartel<sup>15</sup>, and P. Famula<sup>1</sup>

<sup>1</sup> Institut für Astrophysik und Geophysik, Universität Göttingen, Friedrich-Hund Platz 1, 37077 Göttingen, Germany  
e-mail: martin.ochmann@uni-goettingen.de

<sup>2</sup> Ruhr University Bochum, Faculty of Physics and Astronomy, Astronomical Institute (AIRUB), 44780 Bochum, Germany

<sup>3</sup> South African Astronomical Observatory, P.O. Box 9, Observatory Road, Observatory 7935, Cape Town, South Africa

<sup>4</sup> Southern African Large Telescope, P.O. Box 9, Observatory, 7935, South Africa

<sup>5</sup> Department of Astronomy, University of Cape Town, Private Bag X3, Rondebosch 7701, South Africa

<sup>6</sup> Department of Physics, University of the Free State, P.O. Box 339, Bloemfontein 9300, South Africa

<sup>7</sup> Department of Physics, Faculty of Natural Sciences, University of Haifa, Haifa 3498838, Israel

<sup>8</sup> Haifa Research Center for Theoretical Physics and Astrophysics, University of Haifa, Haifa 3498838, Israel

<sup>9</sup> Nicolaus Copernicus Astronomical Center, Polish Academy of Sciences, Bartycka 18, 00-716 Warszawa, Poland

<sup>10</sup> Universidad Católica del Norte, Instituto de Astronomía, Avenida Angamos 0610, Antofagasta, Chile

<sup>11</sup> Department of Physics, Geology, and Engineering Technology, Northern Kentucky University, 1 Nunn Drive, Highland Heights, KY 41099, USA

<sup>12</sup> School of Physics & Astronomy and the Wise Observatory, The Raymond and Beverly Sackler Faculty of Exact Sciences, Tel-Aviv University, Tel-Aviv 69978, Israel

<sup>13</sup> Max-Planck-Institut für Radioastronomie, Auf dem Hügel 69, D-53121 Bonn, Germany

<sup>14</sup> Institute of Astronomy, Madingley Road, Cambridge CB3 0HA, UK

<sup>15</sup> European Space Agency (ESA), European Space Astronomy Centre (ESAC), Villanueva de la Cañada, E-28691 Madrid, Spain

Received 2023 November 10; accepted 2024 February 16

### ABSTRACT

**Context.** NGC 1566 is a local face-on Seyfert galaxy and is known for exhibiting recurrent outbursts that are accompanied by changes in spectral type. The most recent transient event occurred from 2017 to 2019 and was reported to be accompanied by a change in Seyfert classification from Seyfert 1.8 to Seyfert 1.2.

**Aims.** We aim to study the transient event in detail by analyzing the variations in the optical broad-line profiles. In particular, we intend to determine the structure and kinematics of the broad-line region.

**Methods.** We analyzed data from an optical spectroscopic variability campaign of NGC 1566 taken with the 9.2 m Southern African Large Telescope (SALT) between July 2018 and October 2019 triggered by the detection of hard X-ray emission in June 2018. We supplemented this data set with optical to near-infrared (NIR) spectroscopic archival data taken by VLT/MUSE in September 2015 and October 2017, and investigated the emission from different line species during the event.

**Results.** NGC 1566 exhibits pronounced spectral changes during the transient event. We observe the emergence and fading of a strong power-law-like blue continuum as well as strong variations in the Balmer, He I, and He II lines and the coronal lines [Fe VII], [Fe X], and [Fe XI]. Moreover, we detect broad double-peaked emission line profiles of O I  $\lambda$ 8446 and the Ca II  $\lambda$ 8498, 8542, 8662 triplet. This is the first time that genuine double-peaked O I  $\lambda$ 8446 and Ca II  $\lambda$ 8498, 8542, 8662 emission in AGN is reported in the literature. All broad lines show a clear redward asymmetry with respect to their central wavelength and we find indications for a significant blueward drift of the total line profiles during the transient event. The profiles and the FWHM of the Balmer lines remain largely constant during all observations. We show that the double-peaked emission line profiles are well approximated by emission from a low-inclination, relativistic eccentric accretion disk, and that single-peaked profiles can be obtained by broadening due to scale-height-dependent turbulence. Small-scale features in the O I and Ca II lines suggest the presence of inhomogeneities in the broad-line region.

**Conclusions.** We conclude that the broad-line region in NGC 1566 is dominated by the kinematics of a relativistic eccentric accretion disk. The broad-line region can be modeled to be vertically stratified with respect to scale-height turbulence with O I and Ca II being emitted close to the disk in a region with high (column) density, while the Balmer and helium lines are emitted at greater scale height above the disk. The observed blueward drift might be attributed to a low-optical-depth wind launched during the transient event. Except for this wind, the observed kinematics of the broad-line region remain largely unchanged during the transient event.

### 1. Introduction

Variability is widespread in active galactic nuclei (AGN). It occurs in all spectral bands and on typical timescales of hours to weeks or even years. Generally, the variability of AGN is as

<sup>\*</sup> Based on observations made with the Southern African Large Telescope (SALT).

sumed to be stochastic in nature and has been used with great success in the last  $\sim 30$  years to identify and map the innermost AGN structures —namely the accretion disk (AD), the broad-line region (BLR), and the dusty torus (TOR)— using methods such as reverberation mapping (RM; [Blandford & McKee 1982](#)). RM traces the lagging emissive response of individual AGN emission lines to the time-varying ionizing continuum radiation from the central source close to the supermassive black hole (SMBH). As regular and densely sampled observations of the X-ray/UV ionizing continuum are difficult to acquire, an optical continuum is often used as a proxy for the ionizing radiation. Typical optical continuum and line variability for an object (on timescales of months) can span a wide range, from only a few percent up to a few dozen percent (e.g., [Ulrich et al. 1997](#)). Aside from these typical temporal variations of the continuum and emission lines, studies have shown that the variability behavior of individual objects can differ from one epoch to another, and apparent variations of the BLR responsivity have been reported (e.g., [Hu et al. 2020](#); [Gaskell et al. 2021](#)), sometimes over timescales comparable to or even shorter than the expected dynamical timescales ([De Rosa et al. 2018](#)).

In addition to the overall stochastic variability behavior of AGN, transient events such as changing-look (CL) transitions have increasingly gained attention over recent years. Originally, the term “changing-look” was used to describe Compton-thick AGN becoming Compton-thin and vice versa (e.g., [Guainazzi 2002](#); [Matt et al. 2003](#)). In analogy, optical CL AGN are characterized by their change of spectral classification, switching between Sy 1 and Sy 2 and associated subtypes<sup>1</sup>. These transitions happen over timescales of months to years and are often accompanied by significant flux changes on the order of several magnitudes (e.g., [MacLeod et al. 2016](#); [Graham et al. 2020](#); [Green et al. 2022](#)). The observed change between Seyfert types during CL events does not challenge the general validity of the unified AGN model, according to which the source classification is mainly due to the orientation with respect to the observer ([Antonucci 1993](#)). Rather, the huge change in continuum flux on short timescales and the resulting apparent changes in BLR kinematics provide a unique opportunity to refine our understanding of BLR structure. According to the locally optimized cloud model (LOC model [Baldwin et al. 1995](#)), the continuum luminosity determines which parts of the BLR —near or far from the continuum source— are visible. If the BLR is not scale invariant, then a transient event inevitably leads to obvious changes in BLR kinematics and Seyfert subtype. However, to date, the implications of the LOC model have not been adequately addressed in CL-AGN research.

The typical CL transition timescales cannot be explained by viscous radial inflow, a circumstance that is known as the “viscosity crisis” ([Lawrence 2018](#), and references therein). Currently, several explanations for the CL phenomenon are discussed, including tidal disruption events (TDEs), strong variations in the accretion flow, microlensing caused by an intervening object, or sudden changes in obscuration. However, at least for some cases, the behavior of the observed post-CL light curves disfavors discrete events as the cause of the CL phenomenon (e.g., [Runnoe et al. 2016](#); [Zetzl et al. 2018](#)). In general, the similarities between TDEs and some observed CL events require

<sup>1</sup> Sy 1 galaxies show Balmer lines that are wider than the forbidden lines, while Sy 2 galaxies show Balmer lines that are about the same width as the forbidden lines ([Khachikian & Weedman 1974](#)). The types Sy 1.2, Sy 1.5, Sy 1.8, and Sy 1.9 galaxies are subtypes, with numerically larger Seyfert classes showing weaker broad emission with respect to the narrow lines ([Osterbrock 1977, 1981](#); [Winkler 1992](#)).

clearly defined distinction criteria and, in turn, extensive observational data for each event (e.g., [Zabludoff et al. 2021](#); [Komossa & Grupe 2023](#)).

Other possible mechanisms that are discussed include accretion disk instabilities ([Nicastro et al. 2003](#)), magneto-rotational instabilities (e.g., [Ross et al. 2018](#)), radiation pressure instabilities ([Śniegowska et al. 2023](#)), magnetically elevated accretion (e.g., [Dexter & Begelman 2019](#)), accretion state transitions (e.g., [Noda & Done 2018](#)), and interactions between binaries of SMBHs ([Wang & Bon 2020](#)). In addition, the phenomenon of periodicities in AGN light curves (e.g., [Bon et al. 2017](#), and references therein) and repeat CL events (e.g., [Śniegowska et al. 2020](#)) has gained more attention from the scientific community in recent years.

Until recently, CL events were thought to be rather rare. However, the evidence for CL events being much more common has been growing in recent years. To date, a few dozen CL AGN have been identified. Early detections include NGC 1566 ([Pastoriza & Gerola 1970](#)), NGC 3515 ([Collin-Souffrin et al. 1973](#)), NGC 4151 ([Penston & Perez 1984](#)), and Fairall 9 ([Kollatschny & Fricke 1985](#)). More recent detections are, for example, NGC 2617 ([Shappee et al. 2014](#)), Mrk 590 ([Denney et al. 2014](#)), HE 1136-2304 ([Parker et al. 2016](#); [Zetzl et al. 2018](#); [Kollatschny et al. 2018](#)), WISEJ1052+1519 ([Stern et al. 2018](#)), and IES 1927+654 ([Trakhtenbrot et al. 2019a](#)). However, only a few of them —most notably IES 1927+654— have been studied spectroscopically in greater detail in temporal proximity to the transient event. This lack of high-quality data is a significant hindrance to endeavors to understand the CL phenomenon.

NGC 1566 ( $\alpha_{2000} = 04^{\text{h}}20^{\text{m}}00.42^{\text{s}}$ ,  $\delta_{2000} = -54^{\circ}56'16.1''$ ) is a local ( $z = 0.00502$ ) face-on Seyfert galaxy<sup>2</sup> and is known for exhibiting recurrent outbursts accompanied by changes in spectral type ([Shobbrook 1966](#); [Pastoriza & Gerola 1970](#); [Alloin et al. 1985, 1986](#)). The most recent transient event occurred from 2017 to 2019, and an accompanying CL event (a change in Seyfert classification from Sy 1.8 to Sy 1.2; that is, from showing only weak broad emission in H $\beta$  and H $\alpha$  to showing stronger broad H $\beta$  emission) was reported by [Oknyansky et al. \(2019, 2020\)](#). Optical (post-)outburst spectra from 2018 were presented by [Oknyansky et al. \(2019, 2020\)](#) and [Ochmann et al. \(2020\)](#). The flux and spectral variations were the strongest changes observed since 1962, when NGC 1566 exhibited similarly strong broad-line emission ([Shobbrook 1966](#); [Pastoriza & Gerola 1970](#)). The object already started to brighten significantly in September 2017 ([Dai et al. 2018](#)) and reached its peak optical flux in July 2018. A thorough historical overview of the variations in NGC 1566 from the 1960s until today can be found in [Oknyansky et al. \(2020\)](#).

Here, we present first results of a multiwavelength campaign of NGC 1566 during its transient event from 2017 to 2019. Observations with SALT, *XMM*-Newton, NuSTAR, and *Swift* were triggered by the detection of hard X-ray emission with Integral in June 2018 ([Ducci et al. 2018](#)). This led to a dense multiwavelength campaign with a duration of  $\sim 850$  days and follow-up observations in 2019/2020. The first *XMM*-Newton, NuSTAR, and *Swift* observations ([Parker et al. 2019](#)) revealed the rapid increase in X-rays and the presence of a typical Seyfert-1-type X-ray spectrum in outburst, along with the formation of an X-ray wind at  $v \sim 500 \text{ km s}^{-1}$ . In 2023 October, NGC 1566 was found to be in a low state in all *Swift* bands ([Xu et al. 2024](#)). Further results of the observations with *XMM*-Newton, NuSTAR, and *Swift* will be presented in future publications. Our observations

<sup>2</sup> <https://ned.ipac.caltech.edu/>

are supplemented by archival observations with VLT/MUSE, and cover the optical and NIR wavelength range ( $\sim 4300 \text{ \AA} - \sim 9300 \text{ \AA}$ ) at epochs directly before, during, and after the transient event. The observations in detail reveal drastic changes in the line emission and nonstellar continuum. The present paper is structured as follows. In Sect. 2, we describe the observations and the data reduction. In Sect. 3, we present the analysis of the spectroscopic observations. We discuss the results in Sect. 4 and summarize them in Sect. 5. Throughout this paper, we assume a  $\Lambda$  cold dark matter cosmology with a Hubble constant of  $H_0 = 73 \text{ km s}^{-1} \text{ Mpc}^{-1}$ ,  $\Omega_\Lambda = 0.73$ , and  $\Omega_M = 0.27$ .

## 2. Observations and data reduction

### 2.1. Optical spectroscopy with SALT

We acquired optical long-slit spectra of NGC 1566 with the Southern African Large Telescope (SALT; Buckley et al. 2006) at 2 epochs shortly after the detection of hard X-ray emission in June 2018, and one follow-up spectrum in September 2019. The observations have proposal codes 2018-1-DDT-004, 2018-1-DDT-008 (PI: Kollatschny) and 2018-2-LSP-001 (PI: Buckley). The log of the spectroscopic observations is given in Table 1. In addition to the galaxy spectra, we took necessary calibration images (flat-fields, Xe arc frames). All observations were taken under identical instrumental conditions with the help of the Robert Stobie Spectrograph (RSS; Kobulnicky et al. 2003) using the PG0900 grating and a 2x2 spectroscopic binning. To minimize differential refraction, the slit width was fixed to  $2''.0$  projected onto the sky at an optimized projection angle. For the extraction of the spectra, we used a square aperture of  $2''.0 \times 2''.0$ . We covered the wavelength range from 4210 to 7247  $\text{\AA}$  with a spectral resolution of  $\sim 6.7 \text{ \AA}$ . This corresponds to object rest-frame wavelengths of 4189 to 7211  $\text{\AA}$ . Two gaps in the spectra are caused by gaps between the three CCDs of the spectrograph. They range from 5219 to 5274  $\text{\AA}$  and 6262 to 6315  $\text{\AA}$  (5193 to 5248  $\text{\AA}$  and 6231 to 6283  $\text{\AA}$  in the rest-frame), respectively. For all observations, we used the same instrumental setup as well as the same standard star (LTT 4364) for flux calibration, and performed standard reduction procedures using IRAF packages. In order to account for small spectral shifts ( $\lesssim 0.5 \text{ \AA}$ ) in the wavelength calibration between spectra, we performed a wavelength intercalibration with respect to the MUSE spectra. This was done separately for the H $\beta$  and H $\alpha$  line using the narrow lines [O III]  $\lambda\lambda 4959, 5007$  and [S II]  $\lambda\lambda 6716, 6731$ , respectively.

In addition to our three observations, we utilize one additional SALT observation of NGC 1566 from the SALT archive<sup>3</sup> for our variability study. This spectrum was taken on 2018 July 30 as part of the proposal 2018-1-SCI-029 (PI: Marchetti) by the RSS using the PG0900 grating, a  $1''.5$  slit and 2x4 binning. This setup covered the wavelength range from 4920 to 7922  $\text{\AA}$  with a spectral resolution of  $\sim 5.7 \text{ \AA}$ . This corresponds to object rest-frame wavelengths of 4895 to 7882  $\text{\AA}$ . We followed the same reduction steps as for the other SALT observations, employing calibration images with matching instrumental setup. In particular, we used the same standard star LTT 4364 for flux calibration of the spectrum. The signal-to-noise ratio (S/N) in the continuum range ( $5100 \pm 20$ )  $\text{\AA}$  (rest-frame) is  $\sim 110$  compared to S/N  $\sim 190$  in the  $2''.0$  aperture SALT spectrum from 2018 July 20.

All spectra were corrected for Galactic reddening applying the extinction curve of Cardelli et al. (1989) and using a ratio

$R$  of absolute extinction  $A(V)$  to  $E_{B-V} = 0.0079$  (Schlafly & Finkbeiner 2011) of 3.1, and calibrated to the same [O III]  $\lambda 5007$  flux of  $(102 \pm 2) \times 10^{-15} \text{ ergs s}^{-1} \text{ cm}^{-2}$  (see 2.2) in the optical regime. We also corrected for slightly different background flux contributions between observations using an intercalibration to a campaign (Ochmann et al., in prep.) with the UV-Optical Telescope (UVOT; Roming et al. 2005) of *Swift*. The differing background flux contributions arise due to differing observing conditions between observations and the large spatial extent of NGC 1566 in the slit.

**Table 1.** Log of spectroscopic observations of NGC 1566 before, during and after the transient event in 2018.

ID	Mod. JD	UT Date	Exp. Time [s]	Seeing FWHM	Instr.
1	57289.23	2015-09-24	2080	$2''.25$	MUSE <sup>a</sup>
2	58049.20	2017-10-23	3600	$0''.89$	MUSE <sup>b</sup>
3	58319.17	2018-07-20	600	$1''.6$	RSS
4	58329.16	2018-07-30	100	-	RSS
5	58395.96	2018-10-04	600	$1''.9$	RSS
6	58735.03	2019-09-09	600	$1''.5$	RSS

**Notes.**<sup>a</sup> Obtained in no-AO wide field mode.<sup>b</sup> Obtained in AO wide field mode.

### 2.2. Optical and NIR spectroscopy with MUSE

NGC 1566 was observed with VLT/MUSE (Multi Unit Spectroscopic Explorer; Bacon et al. 2010; Bacon et al. 2014) IFU spectrograph as part of the ESO programs 096.D-0263 (PI: J. Lyman) and 0100.B-0116 (PI: C.M. Carollo) on 2015 September 24 and 2017 October 23, respectively. The former observation was carried out in the no-AO wide field mode (WFM), that is, with natural seeing and FoV of  $1' \times 1'$ , while the latter was performed in the AO WFM making use of adaptive optics. MUSE covers the optical and NIR wavelength range between  $\sim 4700 \text{ \AA}$  and  $9300 \text{ \AA}$  at a spectral resolution of  $\sim 2.5 \text{ \AA}$ . The spectra are sampled at  $1.25 \text{ \AA}$  in dispersion direction and at  $0''.2$  in spatial direction. The seeing and exposure time of the observations are given in Table 1.

The data were reduced using the MUSE pipeline development version 1.6.1 and 2.2 (Weilbacher et al. 2012, 2014) for the observation from 2015 September 24 and 2017 October 23, respectively. This reduction includes the usual steps of bias subtraction, flat-fielding using a lamp-flat, wavelength calibration and twilight sky correction. Every data cube is the product of four combined raw science images. We extracted spectra of NGC 1566's nucleus and the H II region detected by da Silva et al. (2017) using circular apertures of  $1''.0$  and  $0''.5$  radius, respectively. The apertures were chosen such that they are centered on the respective region, comprise the bulk of the emission, and have minimal overlap. A zoomed-in region of the data cube from 2017 October 23 centered on the nucleus is shown in Fig. 1. The apertures are indicated by a blue and magenta circle, respectively.

In the following, we use the AO wide field mode MUSE spectrum from 2017 October 23 as a reference spectrum for all spectroscopic observations. Therefore, we calibrated all spectra to the same absolute [O III]  $\lambda 5007$  flux of  $(102 \pm 2) \times 10^{-15} \text{ ergs s}^{-1} \text{ cm}^{-2}$ . This value is in agreement with results of Kriss et al. (1991), who measured an [O III]  $\lambda 5007$  flux of  $(101.62 \pm 7.32) \times$

<sup>3</sup> <https://ssda.saao.ac.za/>

$10^{-15}$  ergs  $\text{s}^{-1}$   $\text{cm}^{-2}$  in a HST/FOS spectrum obtained with an aperture of  $0''.3$  on 1991 February 8. This indicates that the bulk of the  $[\text{O III}] \lambda 5007$  emission close to the nucleus stems from a confined region with a size  $\lesssim 0''.3$ , which translates to  $\lesssim 30$  pc using the Cosmology Calculator of [Wright \(2006\)](#).

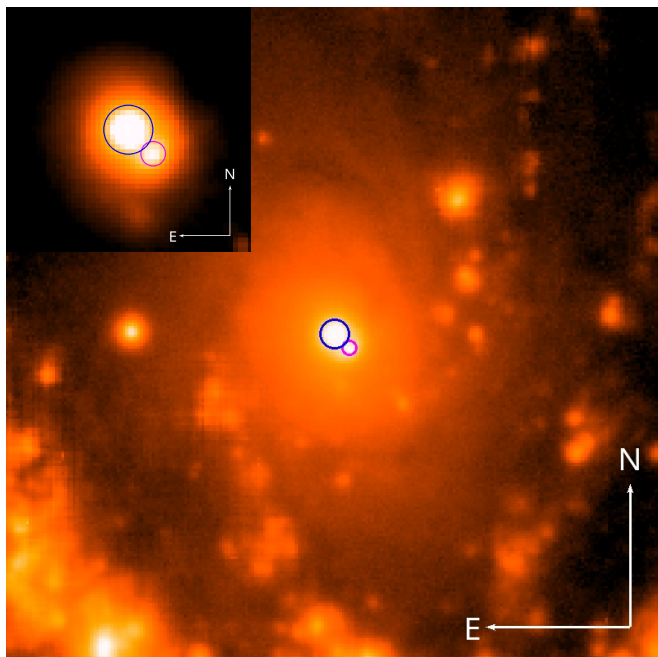


**Fig. 1.** Image ( $45''.0 \times 45''.0$ ) of the central region of NGC 1566 at  $6597 \text{ \AA}$  (observed frame) taken by MUSE on 2017 October 23. Each arm of the compass is  $10''.0$  in length. Spectra of the nucleus and the  $\text{H II}$  region were extracted using apertures of  $1''.0$  and  $0''.5$  in radius, respectively, indicated by the blue and magenta circle. The inlay shows the zoomed-in nuclear region ( $10''.0 \times 10''.0$ ). Each arm of the compass is  $2''.0$  in length. The color scale is logarithmic in order to enhance weaker emission features.

### 3. Results

#### 3.1. Optical spectral observations

We present all reduced optical spectra obtained before, during, and after the transient event in NGC 1566 in Fig. 2. For each spectrum, we give a chronologically sorted ID, the UT date and the time difference in days with respect to 2018 July 02 ( $t_0 = 58301.44$  MJD), when NGC 1566 reached its peak optical flux in the ASAS-SN<sup>4</sup> (All-Sky Automated Survey for Supernovae; [Shappee et al. 2014](#); [Kochanek et al. 2017](#); [Jayasinghe et al. 2019](#)) V-band and g-band light curves.

Spectrum 1 was obtained on 2015 September 24, and therefore  $\sim 700$  days before [Dai et al. \(2018\)](#) reported a brightening of NGC 1566 in September 2017, and 1012 days before the transient event reached its peak. Spectrum 2<sup>5</sup> was obtained on 2017 October 23, 252 days before peak flux. This spectrum sees the emergence of a nearly linear continuum across the optical band, accompanied by the appearance of strong Fe II multiplet emission of the transitions 42 ( $\sim 4910 - 5180 \text{ \AA}$ ), 48 and 49 ( $\sim 5185 - 5450 \text{ \AA}$ ), and weak coronal line emission of

<sup>4</sup> <http://www.astronomy.ohio-state.edu/~assassin>

<sup>5</sup> We note that the narrow component of  $\text{H}\alpha$  in Spectrum 2 obtained with MUSE is affected by overexposure, which considerably reduces the measured flux of  $\text{H}\alpha_{\text{narrow}}$ .

$[\text{Fe VII}] \lambda\lambda 5721, 6087$  and  $[\text{Fe X}] \lambda 6375$  as well as weak emission of  $\text{He I} \lambda\lambda 6678, 7065$ .

Spectra 3 and 4 were obtained on 2018 July 20 and July 30, and therefore 18 and 28 days after peak flux. Spectrum 3 has already been presented by [Ochmann et al. \(2020\)](#), however, it had not been intercalibrated to the other spectra of the campaign (see 2.1). To our knowledge, these two high-state spectra presented here are the optical spectra closest to the transient peak presented in the literature so far (see [Oknyansky et al. 2019, 2020](#)). The two spectra are qualitatively identical and show a strong, power-law-like blue continuum, broad  $\text{He I} \lambda\lambda 5876, 6678, 7065$  emission, strong emission in  $\text{H}\alpha$ , very prominent emission between  $\sim 5100 \text{ \AA}$  and  $\sim 5700 \text{ \AA}$ , usually attributed to Fe II emission, as well as coronal line emission of  $[\text{Fe VII}] \lambda\lambda 5721, 6087$  and  $[\text{Fe X}] \lambda 6375$ . Due to the larger wavelength coverage, Spectrum 3 also reveals strong emission of the Balmer lines  $\text{H}\gamma$  and  $\text{H}\beta$  as well as of  $\text{He II} \lambda 4686$  and the Fe II multiplet transitions 38 and 39 ( $\sim 4500 - 4650 \text{ \AA}$ ).

Spectra 5 and 6 were obtained 95 and 434 days after the transient peak, respectively, and reveal the fading of the strong blue continuum as well as of the broad emission lines. One notable exception from the general fading are the coronal lines  $[\text{Fe VII}] \lambda\lambda 5721, 6087$ , which are stronger in the spectrum from 2018 October 4 than in the high-state spectra obtained 77 and 67 days earlier. The spectrum from 2019 September 9 is approximately on the same level as the low-state spectrum from 2015 September 24, but still shows a slightly stronger continuum blueward of  $\sim 6000 \text{ \AA}$ .

To illustrate the timing of the spectral observations, we show the time stamps of all spectral observations along with the ultraviolet *Swift* UVW2-band light curve in Fig. 3. Further, more detailed results on the spectral variations in NGC 1566 during its transient event from 2017 to 2019 will be presented in future publications ([Kollatschny et al., in prep.](#); [Ochmann et al., in prep.](#)).

#### 3.1.1. Host galaxy contribution

All spectra of NGC 1566 (see Fig. 2) show a strong stellar signature from the underlying host galaxy. This holds especially true for the low-state spectra before and after the outburst, where the stellar signature of the host galaxy clearly dominates the continuum regions of the spectra. In order to determine the host galaxy contribution, we perform a spectral synthesis on Spectrum 1 from 2015 September 24. Of all the spectra in the campaign, this spectrum is the most suitable as it has the largest spectral coverage from  $\sim 4700 \text{ \AA}$  to  $9300 \text{ \AA}$  and the lowest contribution from broad-line emission and nonstellar continuum. The way we proceed is identical to that presented for IRAS 23226-3843 by [Kollatschny et al. \(2023\)](#). We use the Penalized Pixel-Fitting method (pPXF) ([Cappellari & Emsellem 2004](#); [Cappellari 2017](#)) and restrict the synthesis to wavelength ranges free from emission lines. This excludes in particular the Fe II complex at  $\sim 5300 \text{ \AA}$  from the fitting procedure. We used the stellar templates from the Indo-US library ([Valdes et al. 2004](#); [Shetty & Cappellari 2015](#); [Guérou et al. 2017](#)), which provides high-enough spectral resolution, and fully covers the wavelength range of interest. In addition to the stellar templates, we add a constant component  $F_\lambda = c$  mimicking a very weak power-law component  $F_\lambda \propto \lambda^{-\beta}$  as the underlying nonstellar AGN continuum. This seems to us to be a reasonable estimate, since we cannot make an a priori statement about the nonstellar spectral index in the low-state spectrum and

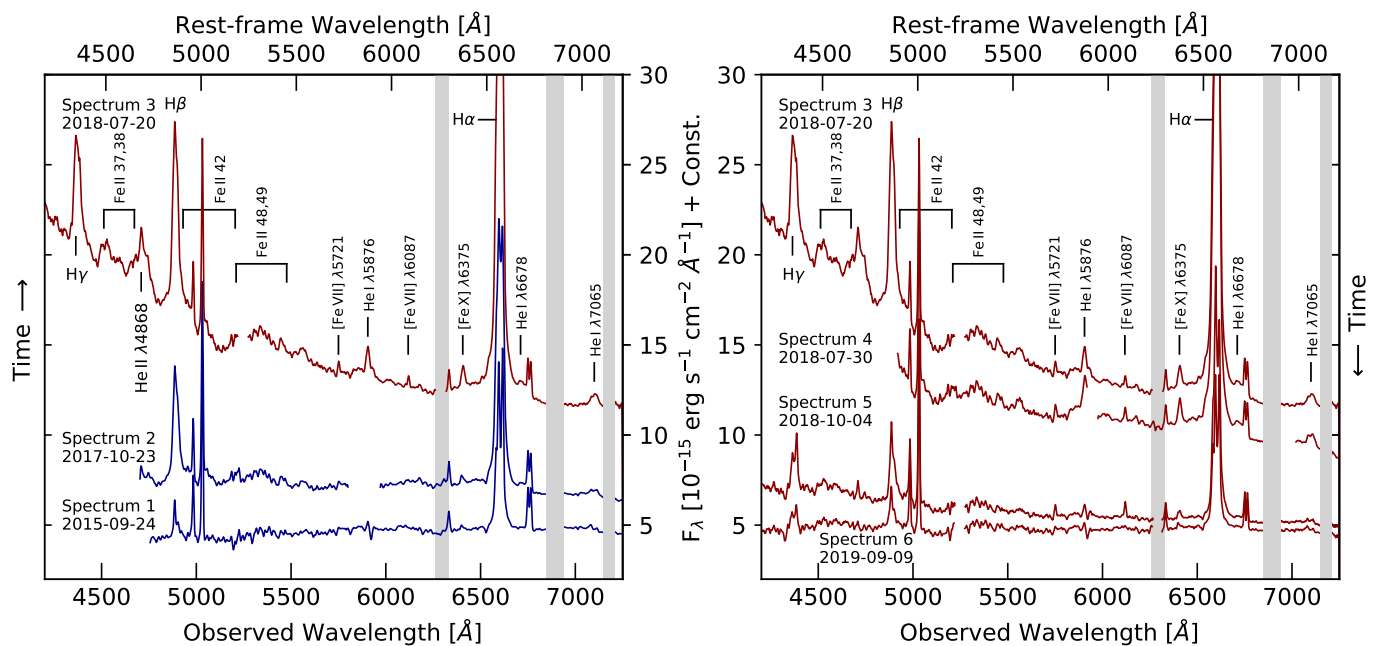


**Fig. 2.** All optical spectra obtained before, during, and after the transient event in NGC 1566. MUSE and SALT spectra are shown in blue and red, respectively. The left panel shows the spectra obtained during the rising phase, including the optical spectrum from 2018 July 20, while the right panel shows the spectra obtained during the declining phase, again including the optical high-state spectrum from 2018 July 20 for reference. The SALT spectrum from 2018 July 30 is shifted by  $-2 \times 10^{-15} \text{ erg s}^{-1} \text{ cm}^{-2} \text{ \AA}^{-1}$  for clarity. For each spectrum, we give the ID as well as the UT date of the observation. The most prominent telluric absorption bands are flagged (gray).

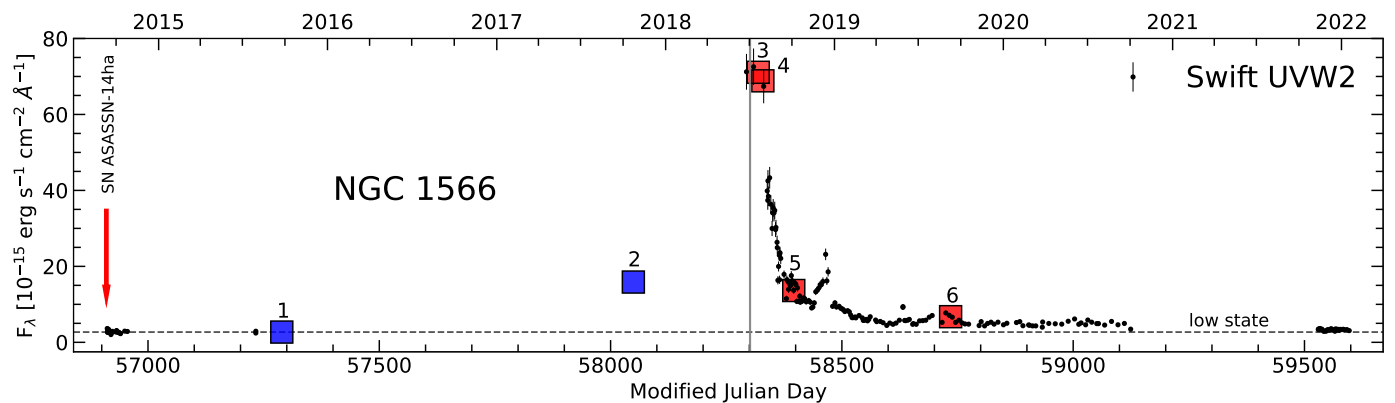


**Fig. 3.** Long-term UV *Swift* UVW2-band light curve before, during, and after the transient event in NGC 1566 from 2017 to 2019. The blue and red boxes mark the time stamps of the spectroscopic MUSE and SALT observations, respectively, and are numbered chronologically. To guide the eye, the boxes are positioned such that they overlap with the UVW2 light curve; that is to say, they do not represent the actual optical flux values, but give a basic representation of the relative flux with respect to each other. The date of detection of the supernova ASASSN-14ha is indicated by a red arrow and the date of peak flux in the ASASSN light curve is shown by a gray line. The pretransient low-state flux level is indicated by a dashed black line.

the contribution of a very weak power law can be approximated as constant in the optical regime.<sup>6</sup>

The result of the spectral synthesis is shown in Fig. 4 together with the input spectrum and the residual spectrum, which is the clean nuclear spectrum of NGC 1566 during its low state. The residual spectrum already includes the approximately constant nonstellar AGN component  $F_{\lambda} = 1.4 \times 10^{-15} \text{ erg s}^{-1} \text{ cm}^{-2} \text{ \AA}^{-1}$ . This allows us to estimate the host galaxy contribution in the original low-state spectrum to be  $\sim 60\%$  and  $\sim 70\%$  in the B

<sup>6</sup> We also note that when presented the possibility to choose from a range of power laws with different indices, pPXF always prefers the power law with the smallest index.

and V band, respectively. The clean low-state nuclear spectrum reveals line features formerly suppressed by the signature of the stellar population in the original spectrum. These features include, amongst others, narrow-line emission of [N I]  $\lambda 5198$ , Fe II emission of the transitions 42, 48, and 49, weak He I  $\lambda\lambda 5876$ , 6678, 7065 emission, and Ca II  $\lambda\lambda 8498$ , 8542, 8662 triplet emission, as well as emission of O I  $\lambda 8446$ .

pPXF determines a stellar velocity dispersion of  $\sigma_{*} = 98^{+12}_{-9} \text{ km s}^{-1}$ . The exact value depends on the choice of the boundary conditions, namely the inclusion or exclusion of the NIR Ca II triplet and the probed wavelength region. We determined the error margins by reasonably varying the boundary conditions, that is, slightly varying the probed wavelength re-

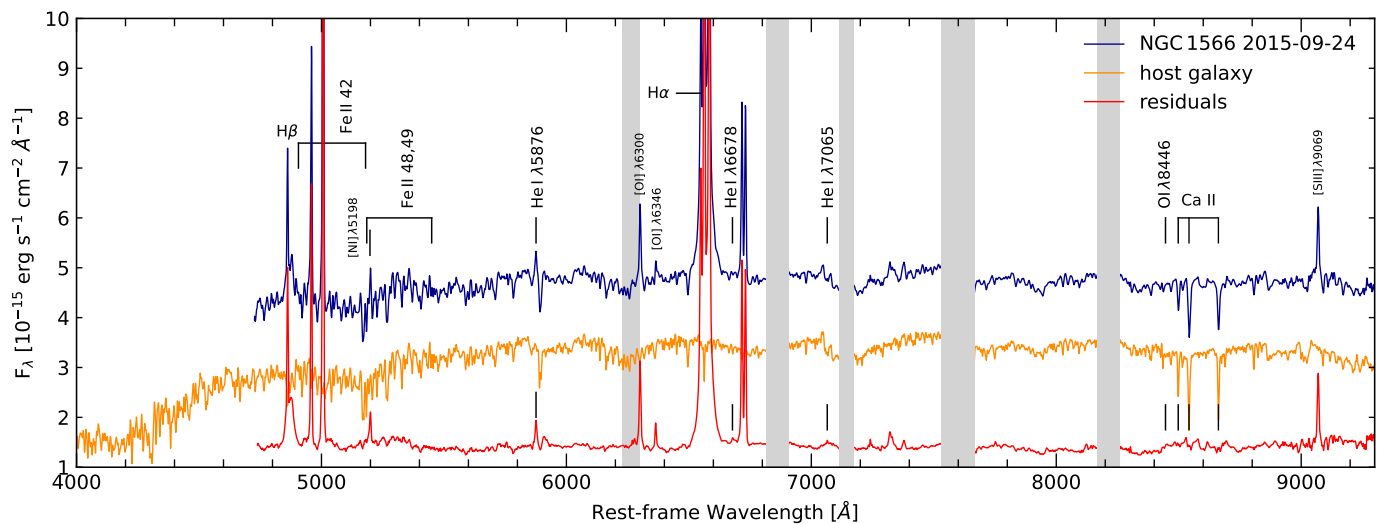


**Fig. 4.** MUSE spectrum of NGC 1566 taken on 2015 September 24 (Spectrum 1; blue) and the synthesis fit of the stellar contribution with pPXF (orange). The residuals (red) give the clean nuclear emission lines spectrum. For the fit, we flagged all prominent line emission including the Fe II complex at  $\sim 5300$  Å. The most prominent telluric absorption bands are flagged (gray).

gions ( $\pm 50$  Å), probing only the optical or NIR part, and excluding or including the NIR Ca II triplet, thereby obtaining a robust range of variation for  $\sigma_*$ . We note that the MUSE spectrum from 2017 October 23, although obtained under favorable seeing conditions, is not suitable to determine an estimation  $\sigma_*$ . In this spectrum, the most prominent absorption feature, namely the Ca II absorption triplet, is blended with Ca II emission, and many wavelength bands are affected by newly emerging line emission (see 3.1 and 3.2). This limits the spectral range with a clean host-galaxy signature and introduces a large scatter in the distribution of determined stellar velocity dispersions  $\sigma_*$ .

### 3.1.2. Balmer line profiles and their evolution

In order to obtain clean nuclear line profiles, we subtract the synthetic host-galaxy spectrum (see 3.1.1) from each spectrum after correcting all spectra to the same dispersion. The resulting host-free, singular-epoch line profiles of H $\beta$  and H $\alpha$  are shown in Fig. 5, where we indicate the central wavelength of H $\beta$  and H $\alpha$  with a dashed line. In order to show the accuracy of the wavelength calibration, which is on the order of  $\pm 20$  km s $^{-1}$ , we likewise indicate the central wavelengths of [O III]  $\lambda 4959, 5007$  and [S II]  $\lambda 6716, 6731$ , respectively. Both the H $\beta$  and the H $\alpha$  profiles show a pronounced redward asymmetry during all phases of the transient event, with no major changes in the overall line profile. This was also observed by Alloin et al. (1985), who found the same redward asymmetry and no significant line profile variations despite considerable flux changes during their optical variability campaign of NGC 1566 from 1980 to 1982. Kriss et al. (1991) reported redshifts of 200–1000 km s $^{-1}$  for all broad lines in their UV to optical FOS/HST spectra.

In order to assess the line profile variations of H $\beta$  and H $\alpha$  in more detail, we calculate the host-free mean and rms line profiles. The resulting profiles are shown in Fig. 6. The H $\beta$  and H $\alpha$  rms profiles, which map only the variable part of the line emission, show no evidence of residual narrow-line flux from H $\beta_{\text{narow}}$ , [O III]  $\lambda 4959, 5007$  (see also 3.3) and H $\alpha_{\text{narow}}$ , [N II]  $\lambda 6548, 6583$ , respectively. This illustrates the high accuracy of the spectral intercalibration. The profiles have a FWHM of  $(2180 \pm 50)$  km s $^{-1}$  and  $(2060 \pm 50)$  km s $^{-1}$  for H $\beta$  and H $\alpha$ ,

respectively, and are strongly asymmetric with respect to the rest-frame velocity, with the red wing being broader by about  $\sim 400$  km s $^{-1}$  with respect to the central wavelength. In addition, both rms profiles show an additional narrow peak component that is not associated with narrow-line residuals, but instead is shifted with respect to the rest-frame central wavelength by  $(220 \pm 50)$  km s $^{-1}$  and  $(210 \pm 50)$  km s $^{-1}$ , respectively. With respect to the peak positions, the central rms profiles are almost perfectly symmetric. Major deviations from symmetry are only evident in the extended line wings.

At this point, the individual H $\beta$  and H $\alpha$  line profiles still comprise contributions from the narrow components H $\beta_{\text{narow}}$  and H $\alpha_{\text{narow}}$  as well as [N II]  $\lambda 6548, 6583$ , respectively. Therefore, in order to obtain clean FWHM measurements for singular epochs, we subtract a scaled [O III]  $\lambda 5007$  profile taken from the 2015 September 24 spectrum as a mean template for each narrow-line component from the total line profile. We adopt this procedure as we explicitly assume that the narrow-line components are not purely Gaussian, but instead are more complex as they are being shaped by the kinematics of the narrow-line region. This is supported by the findings of Alloin et al. (1985) and da Silva et al. (2017), who found that adequately modeling the narrow lines in NGC 1566 requires at least two Gaussians.

We show the resulting broad H $\beta$  line profiles after subtraction of a suitable linear pseudo-continuum in Fig. 7. From each of these profiles, we subtracted a constant narrow-line component H $\beta_{\text{narow}}$  with a flux of  $18.2 \times 10^{-15}$  ergs s $^{-1}$  cm $^{-2}$ . We give the measured FWHM and redshift of all H $\beta_{\text{broad}}$  profiles in Table 2. We observe the following trends in the emission lines: The H $\beta$  profiles in Spectrum 1, Spectrum 2 and Spectrum 3 are skewed and clearly display the redward asymmetry mentioned previously. While the H $\beta_{\text{broad}}$  profile in Spectrum 1 exhibits minor distortions of the central profile, probably due H $\beta_{\text{narow}}$  residuals (see also 3.3), the profile in Spectrum 2 appears to be free from this effect. Most strikingly, we observe a substantial change in redshift of the H $\beta_{\text{broad}}$  profile between Spectrum 1 and Spectrum 2, with a shift of the line peak from  $+(730 \pm 50)$  km s $^{-1}$  to  $+(490 \pm 50)$  km s $^{-1}$ . This trend continues until Spectrum 3, where the redshift of the profile only amounts to  $+(360 \pm 50)$  km s $^{-1}$ . We term this velocity shift of the total H $\beta$  profile during the rising

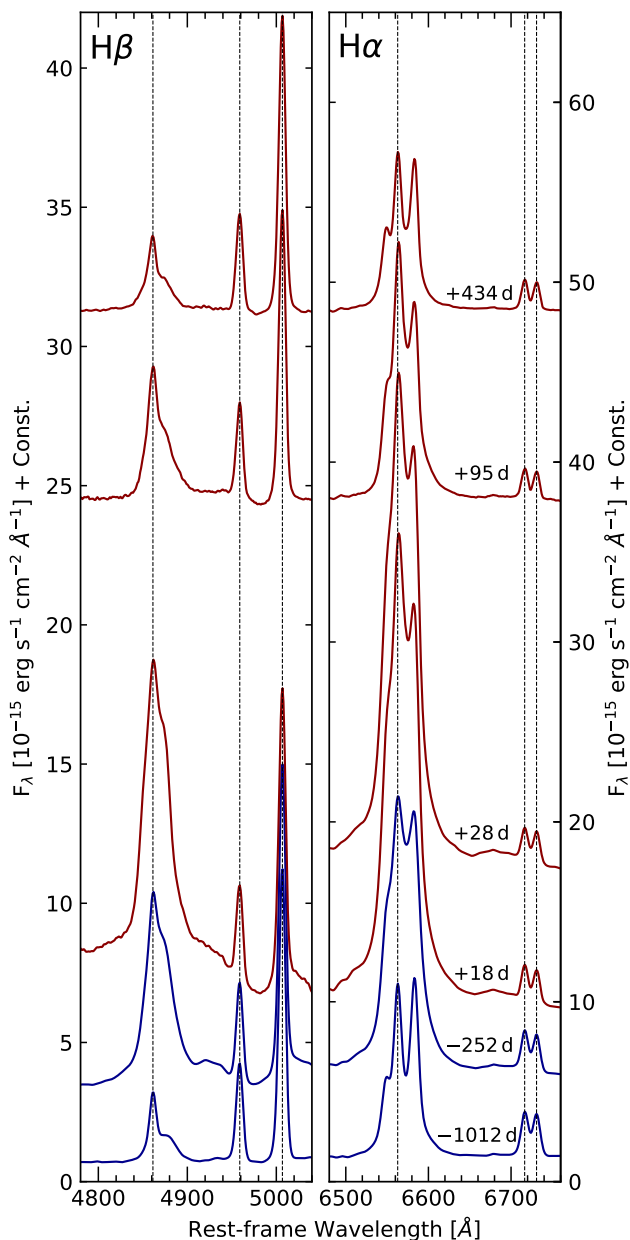


**Fig. 5.** Temporal evolution (from bottom to top) of the host-free line profiles of  $H\beta$  (left panel) and  $H\alpha$  (right panel). MUSE spectra are shown in blue, SALT spectra are shown in red. The profiles are shifted in flux for clarity. We indicate the central wavelengths of  $H\beta$  and  $H\alpha$  by dashed lines. Likewise, we indicate the central wavelengths of the narrow lines  $[O\text{ III}]\lambda 4959, 5007$  and  $[S\text{ II}]\lambda 6716, 6731$  to demonstrate the accuracy of the spectral calibration.

phase of the transient event to be a *bluward drift* of the line profile. To illustrate we show the normalized  $H\beta$  profiles from Spectrum 1 to Spectrum 3 in Fig. 8.

In comparison to the  $H\beta$  profiles from Spectrum 1 to Spectrum 3, the  $H\beta$  profile in Spectrum 5 is slightly distorted with an apparent additional emission component at  $(130 \pm 10)$   $\text{km s}^{-1}$ . The redshift increases from  $(360 \pm 50)$   $\text{km s}^{-1}$  to  $(450 \pm 100)$   $\text{km s}^{-1}$  from Spectrum 3 to Spectrum 5. The profile in Spectrum 6 is two-peaked, caused by the apparent emission component in Spectrum 5 now being present as an apparent absorption component that distorts the profile. Due to the absorption, the  $H\beta_{\text{broad}}$  profile cannot be normalized to peak height like the pre-

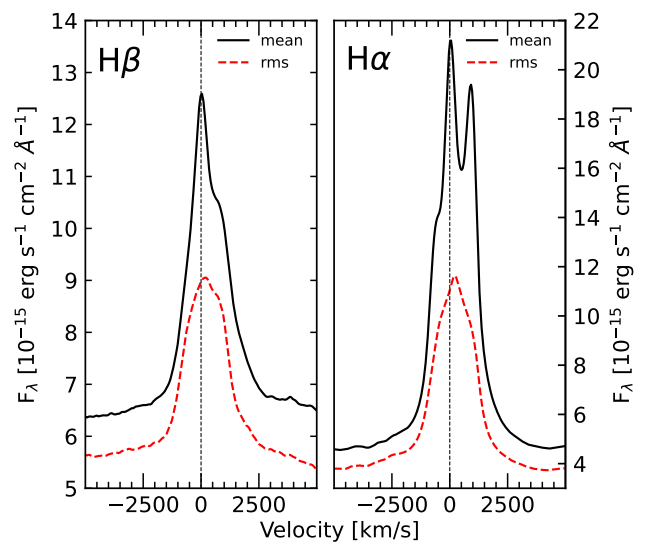


**Fig. 6.** Mean (solid black) and rms (dashed red) line profiles of  $H\beta$  (left panel) and  $H\alpha$  (right panel). The central velocity  $v = 0$   $\text{km s}^{-1}$  is indicated by a black dashed line. The  $H\beta$  and  $H\alpha$  rms profiles show a peak at  $(220 \pm 50)$   $\text{km s}^{-1}$  and  $(210 \pm 50)$   $\text{km s}^{-1}$ , respectively, with respect to the central wavelength. The profiles are strongly asymmetric with the red wing being broader by about  $\sim 400$   $\text{km s}^{-1}$ . The FWHM amounts to  $(2180 \pm 50)$   $\text{km s}^{-1}$  and  $(2060 \pm 50)$   $\text{km s}^{-1}$  for  $H\beta$  and  $H\alpha$ , respectively.

vious profiles, and no meaningful measurement of the redshift can be performed.

**Table 2.** FWHM and redshift  $\Delta v$  (with respect to the central wavelength) of the  $H\beta$  line profile for all epochs.

ID	MJD	UT Date	$(t - t_0)$ [days]	$\text{FWHM}_{H\beta}$ [ $\text{km s}^{-1}$ ]	$\Delta v_{H\beta}$ [ $\text{km s}^{-1}$ ]
1	57289.23	2015-09-24	-1012	$1970 \pm 50$	$+730 \pm 50$
2	58049.20	2017-10-23	-252	$2270 \pm 100$	$+490 \pm 50$
3	58319.17	2018-07-20	+18	$2230 \pm 100$	$+360 \pm 50$
4	58329.16	2018-07-30	+28	-	-
5	58395.96	2018-10-04	+95	$2100 \pm 100$	$+450 \pm 100$
6	58735.03	2019-09-09	+434	$2440 \pm 300$	-

**Notes.** Spectrum 4 from 2018 July 30 does not cover the  $H\beta$  line. The  $H\beta$  profile in Spectrum 6 from 2019 September 09 is distorted and no meaningful normalization of the profile is possible with respect to the other profiles.

Strikingly, the profile and the FWHM of  $H\beta_{\text{broad}}$  do not change significantly during the rising phase of the transient event. The slightly lower value of  $\text{FWHM} = (1970 \pm 50)$   $\text{km s}^{-1}$  in the low-state Spectrum 1 from 2015 September 24 compared to the other spectra is caused by the minor distortion of the central profile due to a narrow-line residual. Taking this residual into account (see 3.3), the width amounts to  $\text{FWHM} = (2200 \pm 50)$   $\text{km s}^{-1}$ , and is therefore in perfect agreement with the values obtained for the other profiles.<sup>7</sup>

Although our procedure is able to recover clean  $H\beta_{\text{broad}}$  profiles, it is not successful in recovering  $H\alpha_{\text{broad}}$  profiles. This is due to differences in the exact profile shape and width between  $[O\text{ III}]\lambda 5007$  and  $[N\text{ II}]\lambda 6548, 6583$ . Nevertheless, because of

<sup>7</sup> We also use the reconstructed profile from 3.3 to determine the redshift of the line.

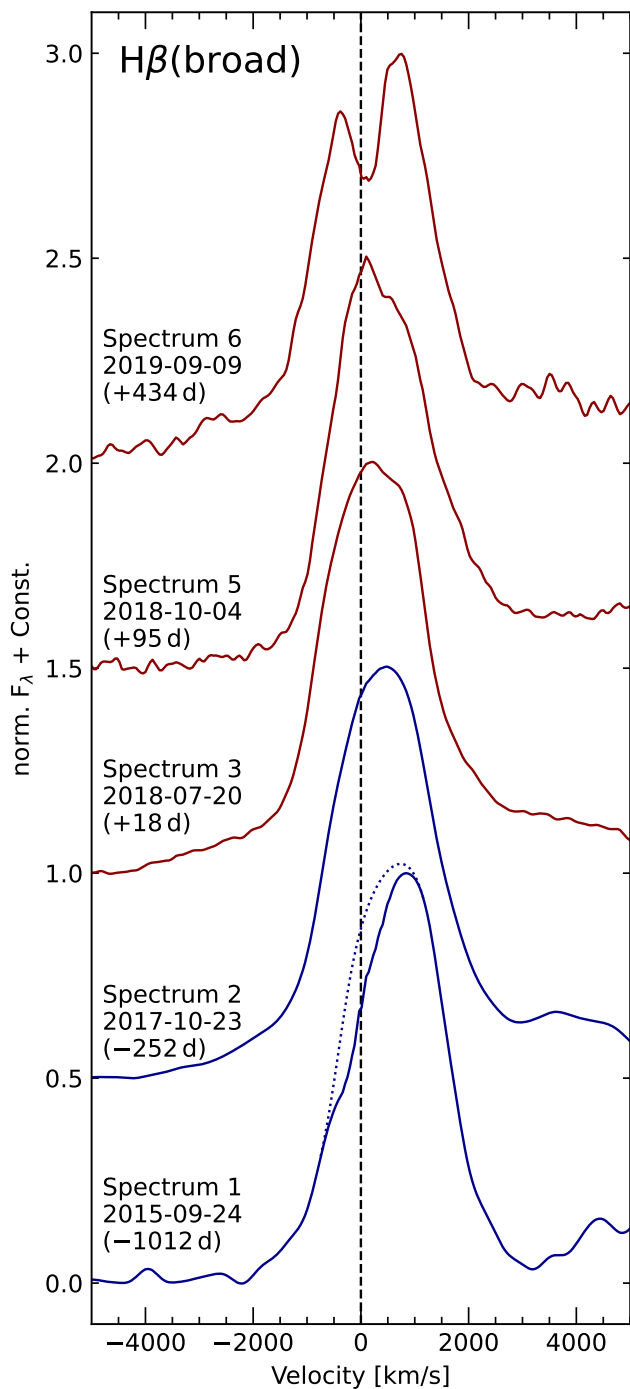


**Fig. 7.** Temporal evolution (from bottom to top) of the normalized, narrow-line, and host-galaxy-subtracted  $H\beta$  profiles in velocity space. A suitable linear pseudo-continuum was subtracted, and the spectra are flux-shifted for clarity. MUSE spectra are shown in blue, SALT spectra are shown in red. The central velocity  $v = 0 \text{ km s}^{-1}$  is indicated by a dashed line. We give the spectrum ID, the date of observations, and the time in days with respect to the peak time  $t_0 = 58301.44 \text{ MJD}$  of the transient event. The reconstructed  $H\beta$  profile for Spectrum 1 (2015 September 24) is shown as a dotted line (see 3.3).

the very similar rms profiles of both  $H\beta$  and  $H\alpha$ , we suspect  $H\alpha_{\text{broad}}$  to show the same behavior as  $H\beta_{\text{broad}}$ .

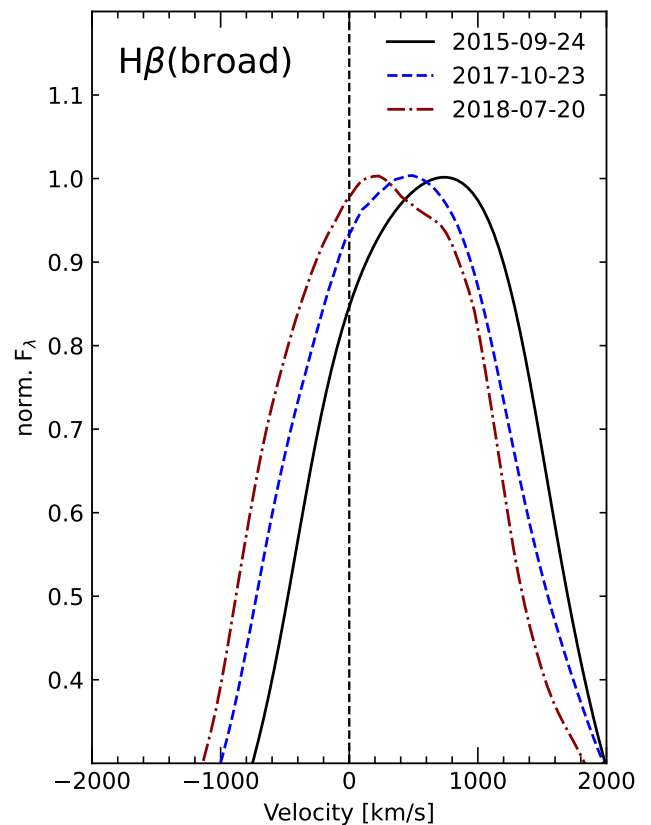


**Fig. 8.** Blueward drift of the normalized  $H\beta$  profiles in velocity space (from Spectrum 1 (2015 September 24) to Spectrum 2 (2017 October 23), and Spectrum 3 (2018 July 20)) after subtraction of the narrow-line and the host-galaxy contribution. The  $H\beta$  profile from Spectrum 1 is the reconstructed  $H\beta$  profile (see 3.3). The blueward drift of the  $H\beta$  profile during the rising phase is clearly visible. The redshift of the  $H\beta$  line shifts from  $(730 \pm 50) \text{ km s}^{-1}$  to  $(490 \pm 50) \text{ km s}^{-1}$  and  $(360 \pm 50) \text{ km s}^{-1}$  from Spectrum 1 to Spectrum 2 and Spectrum 3, respectively.

### 3.1.3. Black hole mass estimation using the $M_{\text{BH}} - \sigma_*$ and $M_{\text{BH}} - \text{FWHM}(H\beta)$ , $L_{5100}$ scaling relations

In 3.1.1, we obtain a value of  $\sigma_* = 98^{+12}_-9 \text{ km s}^{-1}$  for the stellar velocity dispersion in the nuclear region of NGC 1566 during its low state. For the same spectrum we obtain a clean measurement of  $\text{FWHM}(H\beta) = (2200 \pm 50) \text{ km s}^{-1}$  in 3.1.2. These results allow us to estimate the black hole mass  $M_{\text{BH}}$  using the  $M_{\text{BH}} - \sigma_*$  scaling relation of Onken et al. (2004) (see their Eq. 2) and the  $M_{\text{BH}} - \text{FWHM}(H\beta)$ ,  $L_{5100}$  scaling relation of Vestergaard & Peterson (2006) (see their Eq. 5). From the  $M_{\text{BH}} - \sigma_*$  scaling relation we obtain

$$M_{\text{BH}, \sigma_*} = 4.4^{+6.7}_{-2.3} \times 10^6 M_{\odot}. \quad (1)$$

For the  $M_{\text{BH}} - \text{FWHM}(H\beta)$ ,  $L_{5100}$  scaling relation, we measure  $L_{5100}$  in the host-free low-state spectrum. We obtain a continuum flux of  $F_{\lambda} = 1.4 \times 10^{-15} \text{ ergs s}^{-1} \text{ cm}^{-2} \text{ \AA}^{-1}$ , which results in a luminosity of  $\lambda L_{5100} = 3.91 \times 10^{41} \text{ ergs s}^{-1}$ . Together with  $\text{FWHM}(H\beta) = (2200 \pm 50) \text{ km s}^{-1}$  measured in 3.1.2, we therefore obtain a black hole mass of

$$M_{\text{BH}, \text{FWHM}(H\beta), L_{5100}} = 2.5^{+0.2}_{-0.3} \times 10^6 M_{\odot}. \quad (2)$$

Using a velocity dispersion of  $\sigma_* = (105 \pm 10) \text{ km s}^{-1}$ , which is slightly higher than  $\sigma_* = 98^{+12}_-9 \text{ km s}^{-1}$  obtained by us, Smajić et al. (2015) obtained a mass of  $M_{\text{BH}} = (8.6 \pm 4.4) \times 10^6 M_{\odot}$ .



Using also the flux and FWHM of broad Br  $\gamma$  from their data, they estimated the black hole mass  $M_{\text{BH}}$  in NGC 1566 to be  $M_{\text{BH}} = (3.0 \pm 0.9) \times 10^6 M_{\odot}$ , and found their results to be in good agreement with results obtained by [Woo & Urry \(2002\)](#) and [Kriss et al. \(1991\)](#), respectively. We give their results and our values in Table 3. From here on, we adopt the mean black hole mass of  $M_{\text{SMBH}} = (5.3 \pm 2.7) \times 10^6 M_{\odot}$  for NGC 1566.

**Table 3.** Black hole masses  $M_{\text{SMBH}}$  for NGC 1566 determined by different studies. For clarity, we denote if the stellar velocity dispersion  $\sigma_*$  or the FWHM was used for mass determination.

$M_{\text{SMBH}}$ [ $10^6 M_{\odot}$ ]	Method	Reference
4.4 <sup>+6.7</sup> <sub>-2.3</sub>	$\sigma_*$	This work
2.5 <sup>+0.2</sup> <sub>-0.3</sub>	FWHM	This work
8.6 $\pm$ 4.4	$\sigma_*$	<a href="#">Smajić et al. (2015)</a>
3.0 $\pm$ 0.9	FWHM	<a href="#">Smajić et al. (2015)</a>
8.3	$\sigma_*$	<a href="#">Woo &amp; Urry (2002)</a>
5	FWHM	<a href="#">Kriss et al. (1991)</a>
mean		
5.3 $\pm$ 2.7		

### 3.2. Near-infrared spectral observations

MUSE observed NGC 1566 on 2015 September 24 and 2017 October 23 in the wavelength range  $\sim 4700 \text{ \AA}$  to  $9300 \text{ \AA}$ . This is  $\sim 700$  days before and  $\sim 50$  days after the start of the reported brightening of NGC 1566 in September 2017, respectively. We show the NIR part (rest-frame wavelength  $7000 \text{ \AA} - 9300 \text{ \AA}$ ) of the nuclear spectra together with the resulting difference spectrum in Fig. 9. The spectra were extracted using a circular aperture with a radius of  $1''$ . In contrast to the optical regime, the spectra are intercalibrated to the same narrow-line flux of [O II]  $\lambda\lambda 7320, 7330$ , [Ni II]  $\lambda 7378$ , and [S III]  $\lambda 9069$ , as well as the same absorption strength in the Ca II  $\lambda\lambda 8498, 8542, 8662$  triplet. The absorption strength of the Ca II triplet can be considered constant due to the identical aperture of both observations, in other words, the underlying stellar population from the host galaxy is identical.

Spectrum 1 from 2015 September 24 is clearly dominated by the stellar contribution from the host galaxy. The most prominent emission feature in this spectrum are the narrow lines [O II]  $\lambda\lambda 7320, 7330$ , [Ni II]  $\lambda 7378$  and [S III]  $\lambda 9069$ . In addition, prominent absorption in the Ca II  $\lambda\lambda 8498, 8542, 8662$  triplet is present. Spectrum 2 from 2017 October 23, approximately 50 days into the brightening, shows the emergence of a nearly linear continuum across the entire wavelength band, as well as several additional emission lines. Both continuum and line flux can be best recognized in the difference spectrum. We identify broad emission from He I  $\lambda 7065$ , possible emission from Pa 12  $\lambda 8751$ , Pa 11  $\lambda 8863$  (although only marginally detected in both cases) and Pa 9  $\lambda 9229$ , as well as emission from the coronal line [Fe XI]  $\lambda 7892$ , all of which previously not present in the low-state spectrum from 2015 September 24. In addition to the lines identified before, we observe the emergence of broad emission at  $\sim 7306 \text{ \AA}$ , which cannot be unambiguously identified. This broad-line feature might also be present in other NIR AGN spectra (e.g., [Landt et al. 2008](#)), however, a clear detection in

singular-epoch spectra is difficult due to blending with the narrow lines [O II]  $\lambda\lambda 7320, 7330$ .

The most prominent emission feature is broad emission in O I  $\lambda 8446$  and the Ca II  $\lambda\lambda 8498, 8542, 8662$  triplet. We indicate these lines in Fig. 9 by a gray box. The linear continuum subtracted from the line profiles for further analysis is shown by a gray line. A thorough analysis of the line profiles is performed in 3.2.1, 3.2.2 and 3.2.3. We show that the Ca II  $\lambda 8662$  profile is well approximated by emission from an elliptical disk. Furthermore, the blended total profile of O I  $\lambda 8446$  and Ca II  $\lambda\lambda 8498, 8542$  can be reconstructed using the Ca II  $\lambda 8662$  difference profile as a template for all three lines.

#### 3.2.1. The double-peaked Ca II $\lambda 8662$ line profile

We show the clean line profile of Ca II  $\lambda 8662$  in velocity space (after subtraction of the underlying linear continuum indicated in Fig. 9) in Fig. 10. The Ca II  $\lambda 8662$  difference profile is double-peaked, with the red peak being stronger than the blue peak by about 10%. Moreover, the red peak is composed of three individual subpeaks that form a “trident” structure. The total profile is strongly asymmetric with the right wing being broader by  $\sim 300 \text{ km s}^{-1}$ . The full width at half maximum (FWHM) amounts to  $(1920 \pm 50) \text{ km s}^{-1}$  when the Ca II  $\lambda 8662$  profile is normalized to  $F_{\lambda}(0 \text{ km s}^{-1}) = 1$ . The blue and red peak are positioned at  $v_{\text{bluepeak}} \approx -615 \text{ km s}^{-1}$  and  $v_{\text{redpeak}} \approx +950 \text{ km s}^{-1}$ , respectively, and are therefore separated by  $\sim 1600 \text{ km s}^{-1}$ .

The profile closely resembles that of H I 21 cm-line emission profiles in so-called “lopsided” galaxies, where the matter distribution in the galaxy’s plane is asymmetric with respect to the galaxy’s center (e.g., [Richter & Sancisi 1994](#)). Similar asymmetric line profiles have been observed in a number of AGN, for example, Arp 102B ([Popović et al. 2014](#)), NGC 4958 ([Ricci & Steiner 2019](#)), NGC 1097 ([Storchi-Bergmann et al. 1997](#); [Schimoia et al. 2015](#)), and others ([Gezari et al. 2007](#); [Lewis et al. 2010](#)), as well as TDEs, for example, PTF09djl ([Liu et al. 2017](#)), AT 2018hyy ([Hung et al. 2020](#)), AT 2020zso ([Wevers et al. 2022](#)), and are thought to be signatures of an elliptical (accretion) disk. We analyze the line profile of Ca II  $\lambda 8662$  in the framework of an elliptical accretion disk model in 3.2.2 in more detail.

#### 3.2.2. Fitting the Ca II $\lambda 8662$ difference profile with an elliptical accretion disk model

The analysis of the Ca II  $\lambda 8662$  difference profile reveals a strongly asymmetric, double-peaked profile with the red peak being stronger than the blue peak by about 10%. Emission line profiles with stronger red than blue peaks are inconsistent with circular accretion disk models (see, e.g., [Eracleous et al. 1995](#); [Lewis et al. 2010](#)). Instead, they require an asymmetric distribution of matter (or emissivity) in the accretion disk such that the receding part of the disk – with respect to the observer – contributes more to the line flux than the approaching part. We note, however, that observed double-peaked line profiles attributed to the emission from an accretion disk are generally more complex and often additional components such as Gaussians are needed to obtain good fits (e.g., [Hung et al. 2020](#); [Wevers et al. 2022](#)). In general, line profiles in AGN are most likely shaped by a superposition of several effects, such as, amongst many others, the geometry of the BLR, turbulence, (disk) winds (e.g., [Goad & Wanders 1996](#); [Schulz et al. 1995](#); [Goad et al. 2012](#); [Flohic et al.](#)

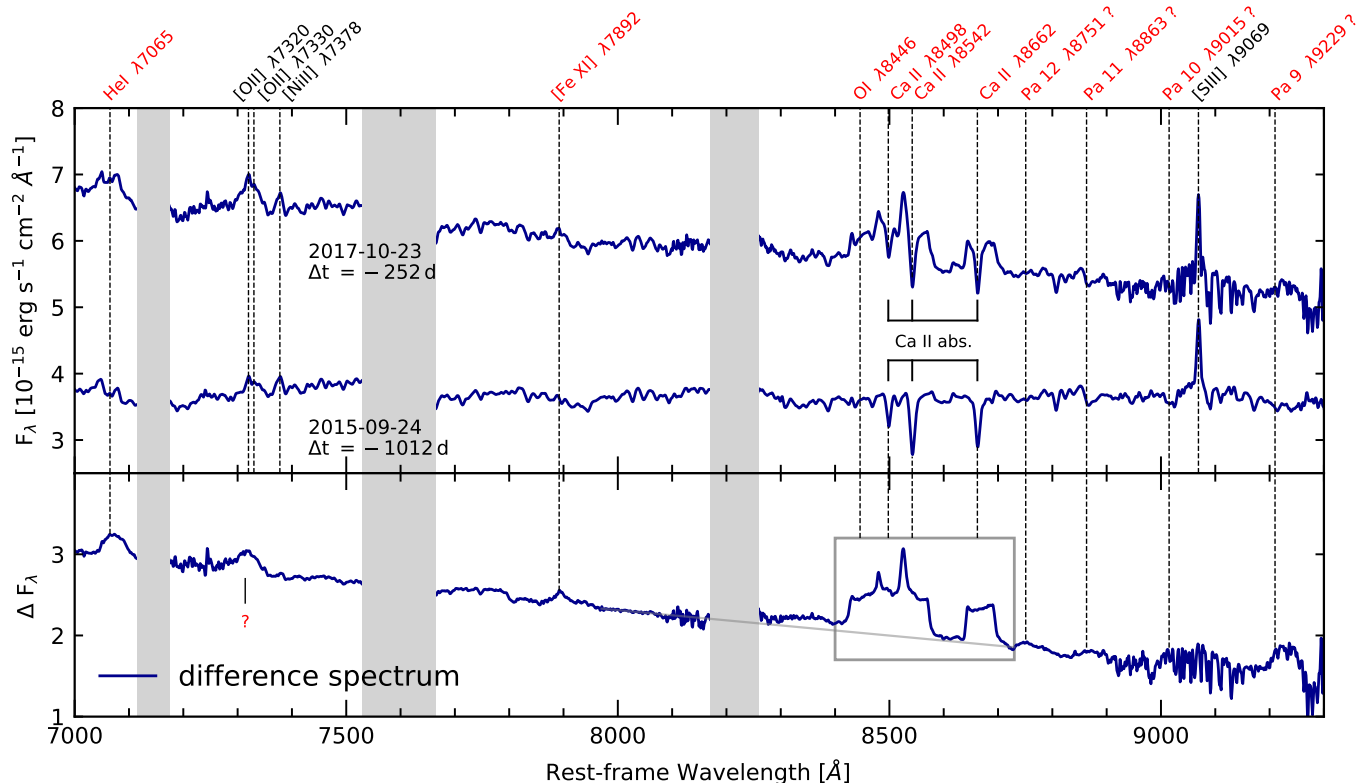


**Fig. 9.** Intercalibrated MUSE NIR spectra from 2015 September 24 and 2017 October 23 (*upper panel*) and the resulting difference spectrum (*lower panel*). The most prominent telluric absorption bands are shown in gray. In addition to an increase in NIR continuum flux, the difference spectrum reveals emission from several broad lines and [Fe xi]  $\lambda 7892$ . The most prominent emission feature is the blend of O I  $\lambda 8446$  and the Ca II  $\lambda 8498$ , 8542, 8662 triplet (gray box). The linear pseudo-continuum used for later analysis is shown as a gray line. The positions of all identified emission lines are marked by dashed lines. Narrow emission lines and the stellar Ca II triplet absorption are denoted in black, while variable line emission is denoted in red.

2012) or, in the case of Ca II  $\lambda 8498$ , 8542, 8662 triplet emission, stellar absorption.

We assume that the Ca II  $\lambda 8662$  profile is indeed a genuine double-peaked profile; that is to say, it is not caused by the underlying stellar absorption of the host galaxy (see 4.2.1 for more details). We therefore fit the Ca II  $\lambda 8662$  line profile with the relativistic elliptical accretion disk model of Eracleous et al. (1995), in which the total observed flux  $F$  from the line is described by the expression

$$F = \int d\nu \int \int d\Omega I_\nu, \quad (3)$$

where  $\nu$ ,  $d\Omega$ , and  $I_\nu$  are the frequency, solid angle element as seen by the observer, and the specific intensity. The specific intensity  $I_\nu$  in the frame of the emitter is given as

$$I_\nu = \frac{1}{4\pi} \frac{\epsilon_0 \xi^{-q}}{\sqrt{2\pi}\sigma} \exp\left[-\frac{(\nu_e - \nu_0)^2}{2\sigma^2}\right], \quad (4)$$

where  $\sigma$  is the broadening parameter,  $\epsilon(\xi) = \epsilon_0 \xi^{-q}$  is the line emissivity, and  $\nu_e$  and  $\nu_0$  are the emitted and rest frequency, respectively. The model has seven free parameters, namely the inner and outer pericenter distance  $\xi_1$  and  $\xi_2$ , the inclination angle  $i$ , the major axis orientation  $\phi_0$ , the broadening parameter  $\sigma$ , the disk eccentricity  $e$ , and the emissivity power-law index  $q$  (see Eracleous et al. (1995) for details).

To find the best-fitting parameter set to the data, we apply a combination of the Monte Carlo method and momentum-based gradient descent to minimize  $\chi^2$  of the model fit. In a first

step, we flag the central part of the profile between  $-450 \text{ km s}^{-1} < \nu < +850 \text{ km s}^{-1}$ , as well as the region for which  $+1350 \text{ km s}^{-1} < \nu < +1750 \text{ km s}^{-1}$ , that is, the inner two peaks of the trident and the outermost red line wing. We proceed in this way as we assume the red trident peak to be a superposition of three individual peaks, all of them with the same width as the blue peak of the Ca II  $\lambda 8662$  profile (see 4.4.3 for details). We then restrict the posterior parameter space by creating  $\sim 250\,000$  models by sampling from a uniform prior parameter distribution of  $200 r_g < \xi_1 < 10\,000 r_g$ ,  $500 r_g < \xi_2 < 20\,000 r_g$ ,  $0^\circ < i < 20^\circ$ ,  $0^\circ \leq \phi_0 < 360^\circ$ ,  $0 \text{ km s}^{-1} < \sigma < 2000 \text{ km s}^{-1}$ ,  $0 \leq e < 1$ , and  $1 < q < 5$ , from which the parameters are randomly drawn. The choice for the inclination  $i$  is based on the results of Parker et al. (2019), who determined an inclination angle of  $i < 11^\circ$ . To scan the parameter space, we first vary individual parameters while leaving the rest of the parameter set fixed. We start with the inclination angle  $i$  and the broadening parameter  $\sigma$ , which mainly govern the width of the total profile and of the blue and red peak, and then investigate the effects of the major axis orientation  $\phi_0$ , the inner and outer pericenter distance  $\xi_1$  and  $\xi_2$ , and finally the disk eccentricity  $e$  and the emissivity power-law index  $q$ . We then examine the parameter space in more detail by iteratively increasing the number of free parameters (up to seven) and varying them with an increasingly finer parameter grid. This iterative approach is similar to the procedure presented by Short et al. (2020).

We find that the only reasonable solutions reproducing the key features of the line profile (namely FWHM, peak width,

and relative peak height) require  $1000 r_g < \xi_1 < 5000 r_g$ ,  $3000 r_g < \xi_2 < 8000 r_g$ ,  $5^\circ < i < 12^\circ$ ,  $150^\circ \leq \phi_0 < 250^\circ$ ,  $50 \text{ km s}^{-1} < \sigma < 200 \text{ km s}^{-1}$ ,  $0.1 \leq e < 0.8$ , and  $2 < q < 5$ . In a second step, we apply the momentum-based gradient descent method to find the minimal value for  $\chi^2$ . In order to exclude running into local minima for  $\chi^2$ , we repeat the run with the momentum-based gradient descent method 1 000 times with start parameters randomly drawn from the restricted prior parameter distribution. We give the best-fit parameter set of the model to our data, in other words, the parameter set from the run that realizes the minimal  $\chi^2$ , in Table 4 and show the resulting model line profile in Fig. 10. The  $\text{Ca II } \lambda 8662$  profile is best modeled with an almost face-on,  $i = (8.10 \pm 3.00)^\circ$ , but eccentric accretion disk with an eccentricity of  $e = (0.57 \pm 0.35)$ , viewed under a major axis orientation of  $\phi_0 = (193.29 \pm 26.00)^\circ$ . The internal broadening to turbulence is low with  $\sigma = (87 \pm 10) \text{ km s}^{-1}$  (corresponding to  $v_{\text{turb}} = 200 \text{ km s}^{-1}$ ), and the emissivity power-law index is  $q = (4.34 \pm 0.80)$ .

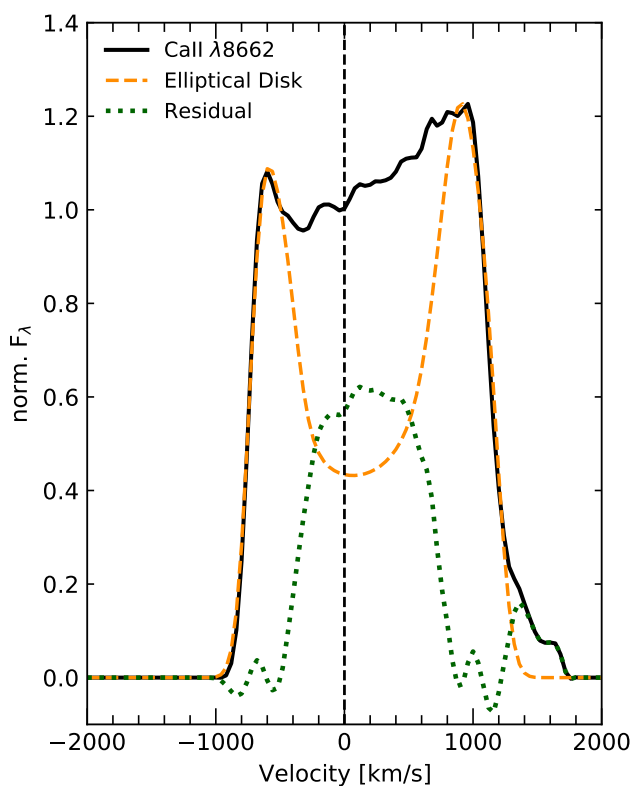


**Fig. 10.** Normalized difference line profile of  $\text{Ca II } \lambda 8662$  in velocity space (black) after subtraction of a linear pseudo-continuum. The profile is double-peaked and strongly asymmetric, with the red peak being stronger (by about 10%) and being shifted to higher velocities ( $v_{\text{redpeak}} \approx +950 \text{ km s}^{-1}$ ) than the blue peak ( $v_{\text{bluepeak}} \approx -615 \text{ km s}^{-1}$ ). In addition, the red peak shows a “trident” structure, meaning, it is composed of three individual subpeaks. The width of the profile amounts to  $\text{FWHM} = (1920 \pm 50) \text{ km s}^{-1}$ . We show the best-fit results for the elliptical disk model (orange) and the residual flux (green).

The blue wing of the  $\text{Ca II } \lambda 8662$  profile is very well approximated by the elliptical disk model, minor deviations are only found at the base of the wing and in the exact height of the peak. While the red wing is in general also well approximated by the best-fit parameter model, the red peak of the model is shifted slightly inwards by about  $50 \text{ km s}^{-1}$ . The central part of the profile between  $-450 \text{ km s}^{-1} < v < +850 \text{ km s}^{-1}$  is not well

approximated by the purely elliptical disk model, and an additional component is clearly visible in the difference profile in Fig. 10. We do not fit the complete line profile by including an additional Gaussian component as has been done in other studies (e.g., Hung et al. 2020; Wevers et al. 2022), since this additional component is clearly not a Gaussian. A thorough discussion of the best-fit results is given in 4.2.2.

### 3.2.3. Decomposing the blended $\text{O I } \lambda 8446$ and $\text{Ca II } \lambda 8662$ profile

We show the blended line profile of  $\text{O I } \lambda 8446$  and the  $\text{Ca II } \lambda \lambda 8498, 8542$  lines (after subtraction of the same linear continuum as for  $\text{Ca II } \lambda 8662$ ) in Fig. 11. The blue wing of  $\text{O I } \lambda 8446$  and the red wing of  $\text{Ca II } \lambda 8542$  are free from other line contributions. The wings have the same profile as the blue and red wing of  $\text{Ca II } \lambda 8662$ , respectively. We therefore suspect that the  $\text{O I } \lambda 8446$  line and the  $\text{Ca II}$  triplet lines in fact all have the same or at least very similar profiles. To test this assumption, we decompose the  $\text{O I } \lambda 8446$ ,  $\text{Ca II } \lambda 8498$  and  $\text{Ca II } \lambda 8542$  complex using the  $\text{Ca II } \lambda 8662$  difference profile as a template for all lines. In fact, we are able to reconstruct the  $\text{O I } \lambda 8446$  and  $\text{Ca II } \lambda \lambda 8498, 8542$  complex using a  $\text{Ca II}$  triplet ratio of 1:1:1 and an  $\text{O I } \lambda 8446$ -to- $\text{Ca II } \lambda 8662$  ratio of 0.85:1. All lines are fixed at their respective central wavelengths ( $\pm 50 \text{ km s}^{-1}$ ). In order to be able to cleanly reconstruct the slope of the blue wing of  $\text{O I } \lambda 8446$ , we have to convolve the  $\text{Ca II } \lambda 8662$  template with a Gaussian with a width corresponding to  $\sigma \approx 70 \text{ km s}^{-1}$ .

The reconstruction using three overlapping  $\text{Ca II } \lambda 8662$  profiles cleanly reproduces the key features of the blend of  $\text{O I } \lambda 8446$  and  $\text{Ca II } \lambda \lambda 8498, 8542$ . In particular, the two peaks in the blended profile can now be clearly attributed to the overlap of  $\text{O I } \lambda 8446$  and  $\text{Ca II } \lambda 8498$ , and of  $\text{Ca II } \lambda 8498$  and  $\text{Ca II } \lambda 8542$ . Only one larger residuum remains in the overlap between the red and blue wing of  $\text{Ca II } \lambda 8498$  and  $\text{Ca II } \lambda 8542$ , respectively. The underlying emission of  $\sim 0.1 \times 10^{-15} \text{ ergs s}^{-1} \text{ cm}^{-2} \text{ \AA}^{-1}$  is on the level of the left continuum after subtraction of the linear pseudo-continuum. We therefore attribute the difference between the reconstructed blended profile and the observed profile to underlying, additional emission not connected to the  $\text{O I } \lambda 8446$  and  $\text{Ca II } \lambda 8498, 8542$  complex.

### 3.3. Reconstructing the Balmer line profiles using the $\text{Ca II } \lambda 8662$ difference profile

We demonstrate in 3.2.3 that the blended line profile of  $\text{O I } \lambda 8446$  and the  $\text{Ca II } \lambda \lambda 8498, 8542$  lines can be decomposed into three individual double-peaked profiles closely resembling that of  $\text{Ca II } \lambda 8662$ . While the  $\text{O I } \lambda 8446$  profile and the  $\text{Ca II } \lambda \lambda 8498, 8542, 8662$  profiles are clearly double-peaked, the Balmer lines show no clear indication of double peaks. Instead, the presented rms profiles of  $\text{H}\beta$  and  $\text{H}\alpha$  indicate single-peaked emission line profiles, but with a similar redward asymmetry as observed in the  $\text{Ca II } \lambda 8662$  difference profile. In the  $\text{H}\beta$  and  $\text{H}\alpha$  rms profiles, the red wing is  $\sim 400 \text{ km s}^{-1}$  broader (with respect to the central wavelength), while the red wing in the  $\text{Ca II } \lambda 8662$  difference profile is  $\sim 300 \text{ km s}^{-1}$  broader than the blue wing.

We now show that the Balmer line profiles can be reconstructed from the  $\text{Ca II } \lambda 8662$  profile by applying a simple broadening function. To this end, we use a three-parameter Lorentzian

$$I(\lambda) = I_0 \left[ \frac{\Gamma^2}{(\lambda - \lambda_0)^2 + \Gamma^2} \right], \quad (5)$$

**Table 4.** Best-fit parameter set for the Ca II  $\lambda 8662$  profile fit using the elliptical disk model of Eracleous et al. (1995).

$\xi_1$ [ $r_g$ ]	$\xi_2$ [ $r_g$ ]	$i$ [deg]	$\phi_0$ [deg]	$\sigma$ [km/s]	$e$	$q$
$2231 \pm 1000$	$4050 \pm 1500$	$8.10 \pm 3.00$	$193.29 \pm 26.00$	$87 \pm 10$	$0.57 \pm 0.35$	$4.34 \pm 0.80$

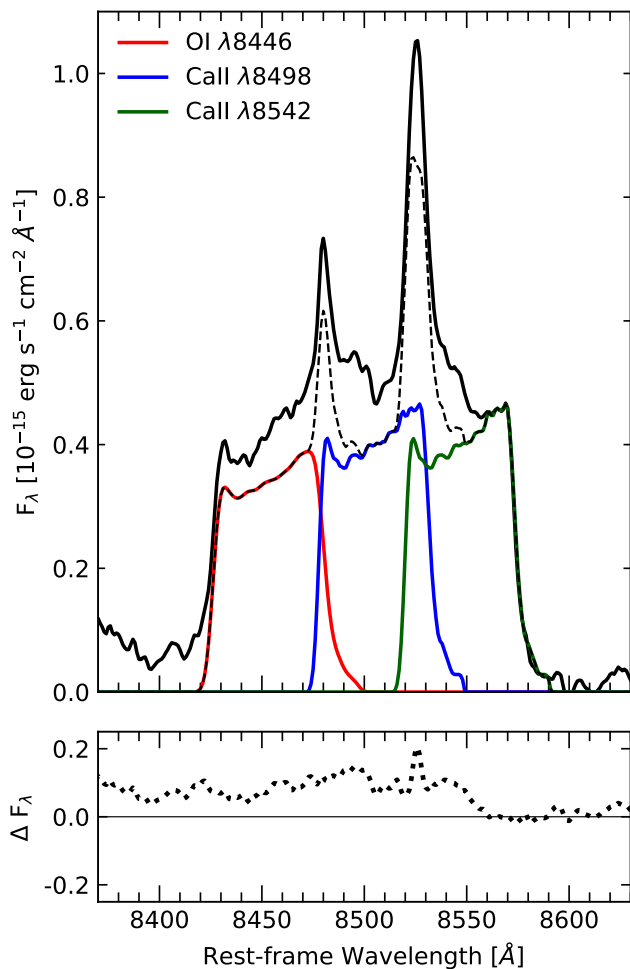


**Fig. 11.** Decomposition of the O I  $\lambda 8446$  and Ca II  $\lambda 8498, 8542$  complex using the Ca II  $\lambda 8662$  line profile (see Fig. 10) as a template for each line constituting the blended profile (black solid line; *upper panel*). We are able to reconstruct the O I  $\lambda 8446$  and Ca II  $\lambda 8498, 8542$  complex using a Ca II triplet ratio of 1:1:1 and an O I  $\lambda 8446$ -to-Ca II  $\lambda 8662$  ratio of 0.85:1. In order to be able to cleanly reconstruct the slope of the blue wing of O I  $\lambda 8446$ , we have to convolve the Ca II  $\lambda 8662$  template with a Gaussian with a width corresponding to  $\sigma = 70 \text{ km s}^{-1}$ . The difference between original blended line profile (black solid line) and reconstructed line profile (black dashed line) is shown in the *lower panel*.

where  $\Gamma$  is the half width at half-maximum. This procedure is motivated by the findings of Kollatschny & Zetzl (2011), who were able to model turbulent motions in the BLR using Lorentzian line profiles, and of Goad et al. (2012), who found that in their bowl-shaped BLR model, Lorentzian line profiles emerge in low-inclination systems for lines formed at larger BLR radii and in the presence of scale-height-dependent turbulence. Therefore, according to the aforementioned models, the broadening by a Lorentzian function in our approach mimics the effects of turbulence in the BLR gas. In addition, other studies also found that emission line profiles in AGN exhibiting line widths

of  $\text{FWHM} \lesssim 4000 \text{ km s}^{-1}$  are well approximated by Lorentzian profiles (e.g., Véron-Cetty et al. 2001; Sulentic et al. 2002).

For this procedure, we use the H $\beta$  line profile from Spectrum 1 (2015 September 24) as well as the H $\beta$  and H $\alpha$  rms profiles. For each of these profiles, we broaden the Ca II  $\lambda 8662$  profile by choosing an appropriate half width  $\Gamma$  such that the broadened Ca II profile matches the corresponding Balmer line profile. In addition, we introduce a velocity shift  $\Delta v$  in order to account for additional blueshifts and redshifts, respectively, of the Balmer lines. The resulting fits and the residual fluxes are shown in Fig. 12. The H $\beta$  line profile from 2015 September 24 is very well approximated by a Ca II  $\lambda 8662$  line profile that is shifted by  $\Delta v = +360 \text{ km s}^{-1}$  and broadened with a Lorentzian with a half width of  $\Gamma = 450 \text{ km s}^{-1}$ . The only major residuum is a small narrow H $\beta$  component. The H $\beta$  rms profile is also well approximated by applying Lorentzian broadening of half width  $\Gamma = 450 \text{ km s}^{-1}$ , but this time with a shift of  $\Delta v = -50 \text{ km s}^{-1}$ . In addition to He II  $\lambda 4686$ , which is already clearly visible in the rms spectrum, we detect emission features at  $\sim 4812 \text{ \AA}$ ,  $\sim 4922 \text{ \AA}$  and  $\sim 5016 \text{ \AA}$  in the residual flux in Fig. 12. Based on the resemblance between the emission features at  $\sim 4922, 5016 \text{ \AA}$  and the difference line profile of He I  $\lambda 7065$  (see Fig. 9), we identify these emission lines as He I  $\lambda 4922, 5016$ . The profiles of He I  $\lambda 4922, 5016, 7065$  as well as of the unidentified emission feature at  $\sim 4812$  are analyzed in more detail in 3.4. The central H $\alpha$  rms profile is again well approximated by applying Lorentzian broadening of half width  $\Gamma = 450 \text{ km s}^{-1}$  with a shift of  $\Delta v = -60 \text{ km s}^{-1}$ . However, the line wings are less well approximated and residuals between  $-2500 \text{ km s}^{-1}$  and  $+2500 \text{ km s}^{-1}$  are clearly visible in the residual flux. In contrast to H $\beta$ , the residual flux in H $\alpha$  indicates an additional and very broad component with a full width at zero intensity (FWZI) of  $\text{FWZI} \sim 20\,000 \text{ km s}^{-1}$ . This is in agreement with the results of Alloin et al. (1986), who found that the broad H $\alpha$  line in NGC 1566 line consisted of two components, namely a broad component with an intermediate width of  $\text{FWHM} = 1910 \text{ km s}^{-1}$  and a much broader component with a width of  $\text{FWHM} = 6200 \text{ km s}^{-1}$ .

### 3.4. Helium line profiles

We show the rms profiles of He I  $\lambda 5016$  as well as of the unidentified emission at  $4812 \text{ \AA}$ , and the difference line profile of He I  $\lambda 7065$  in Fig. 13. In each case, we subtracted a suitable linear pseudo-continuum. All three emission lines have an identical width of  $\text{FWHM} \approx 2170 \text{ km s}^{-1}$  and show indications of a double-peak structure with the red peak again being stronger than the blue peak. The peaks are positioned at  $-615 \text{ km s}^{-1}$  and  $+950 \text{ km s}^{-1}$ , and are therefore identical to the peak positions in Ca II  $\lambda 8662$  (see 3.2.1). In addition, we again observe a redward asymmetry with the red wing being broader by  $\sim 400 \text{ km s}^{-1}$  with respect to the central velocity.

In contrast to Ca II  $\lambda 8662$  (see Fig. 10), the three profiles (see Fig. 13) do not exhibit a central and skewed dip, but instead show additional emission in the region  $-450 \text{ km s}^{-1} < v < +550 \text{ km s}^{-1}$ . Supposing that this additional compo-

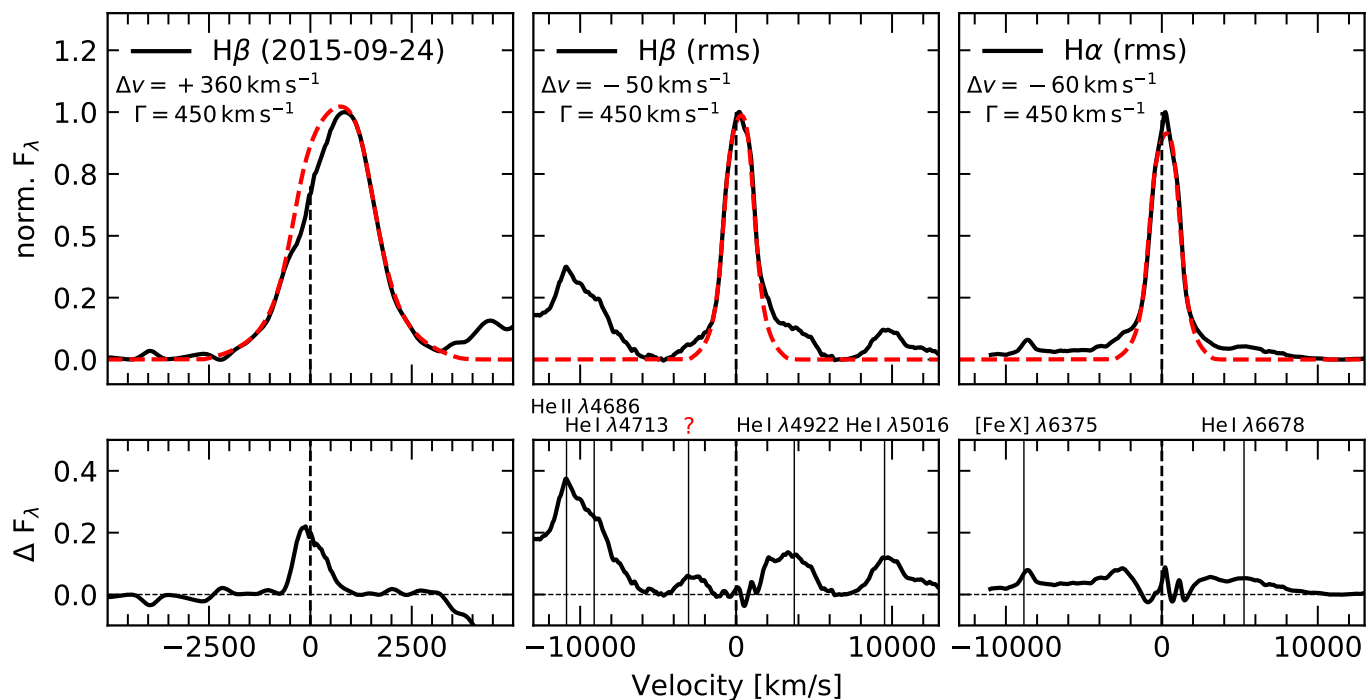


**Fig. 12.** Reconstruction of the H $\beta$  and H $\alpha$  line profiles using the Ca II  $\lambda 8662$  line profile, appropriately shifted by a velocity difference  $\Delta v$  and broadened with a Lorentzian function of half width  $\Gamma$ . The resulting smoothed profiles are shown by a dashed red line (*top panels*). The residual fluxes are shown in the *lower panels*. The residual flux of the H $\beta$  profile from Spectrum 1 (2015 September 24) reveals a small residuum from narrow H $\beta$  emission (*lower left panel*). The residual flux of the reconstructed H $\beta$  rms profile reveals underlying He I  $\lambda 4922$  emission and possible emission from an unidentified line species at  $4812 \text{ \AA}$  (*lower middle panel*). While the central rms profile of H $\alpha$  rms is well approximated by a shifted and broadened Ca II  $\lambda 8662$  difference profile, we see indications for an additional underlying and extremely broad component in the residual flux (*lower right panel*).

ment is superimposed on a double-peaked profile similar to that of Ca II  $\lambda 8662$ , the FWHM of the genuine double-peaked He I  $\lambda 5016$ , 7065 without the additional component can be estimated to be closer to FWHM  $\sim 2500 \text{ km s}^{-1}$ .

### 3.5. The H II region close to the nucleus

An H II region at a separation of only  $\sim 1''0$  (corresponding to  $\sim 100 \text{ pc}$ ) from the nucleus of NGC 1566 was detected by Smajić et al. (2015) and da Silva et al. (2017). Due to the close proximity to the nucleus, we investigate the possible extent of contamination from this region in the nuclear spectra. For this purpose, we extract the spectrum of the H II region from the MUSE data cubes from 2015 September 24 and 2017 October 23, respectively, using a circular aperture of  $0''.5$ . Due to the favorable seeing conditions on 2017 October 23 and the spectrum being taken in AO wide field mode, we scale the spectrum from 2015 September 24 to the integrated [O III]  $\lambda 5007$  flux of  $(4.2 \pm 0.3) \times 10^{-15} \text{ ergs s}^{-1} \text{ cm}^{-2}$  from 2017 October 23. The spectra are shown in Fig. 14 together with the resulting difference spectrum. Both spectra are dominated by narrow line emission of H $\beta$   $\lambda 4861$ , [O III]  $\lambda \lambda 4959, 5007$ , [N II]  $\lambda \lambda 6548, 6583$ , H $\alpha$   $\lambda 6563$ , [S II]  $\lambda \lambda 6716, 6731$ , [S III]  $\lambda 9069$ , absorption of the Ca II triplet, and a strong underlying stellar contribution. For the low-state spectrum from 2015 September 24, the V-band flux amounts to  $\sim 0.3 \times 10^{-15} \text{ ergs s}^{-1} \text{ cm}^{-2} \text{ \AA}^{-1}$ . The spectra reveal an apparent increase in flux from 2015 September 24 to 2017 October 23, both in the most prominent narrow lines except for [O III]  $\lambda \lambda 4959, 5007$  as well as in the underlying continuum emission. We attribute this to narrow-line flux losses in the

extended narrow-line region (NLR) due to unfavorable seeing conditions on 2015 September 24 on the one hand, and scattered radiation from the brightening nucleus on 2017 October 23 on the other hand. The effect of the stray emission from the brightening nucleus is best seen in the H $\beta$  line, where a small broad component appears to emerge on 2017 October 23.

## 4. Discussion

### 4.1. Influence of the H II region on the AGN spectra

Stray emission from the H II region at a distance of  $\Delta d \sim 1''0$  from the nucleus can in principle affect the observed AGN spectra by contributing additional continuum and line flux, thereby also affecting the intercalibration of the AGN spectra on the basis of the [O III]  $\lambda 5007$  line. In order to assess the potential effect of stray emission, we inspect the MUSE H II region spectra from 2015 September 24 and 2017 October 24 in 3.5 and determine an integrated [O III]  $\lambda 5007$  flux of  $(4.2 \pm 0.3) \times 10^{-15} \text{ ergs s}^{-1} \text{ cm}^{-2}$ . This is 4% of the integrated [O III]  $\lambda 5007$  of the nuclear region. However, since the extraction apertures for the nuclear region and the H II region in the MUSE spectra were chosen such that the overlap between the apertures is minimal (see 2.2), the real contribution from additional [O III]  $\lambda 5007$  from the H II region can be securely estimated to be  $< 1\%$ , even when taking into account seeing effects. For the SALT spectra, the square aperture of  $2''0 \times 2''0$  for the nuclear region slightly increases the contribution from the H II region, and modest inaccuracies in the exact slit pointing might add to this effect. Nevertheless, the additional contribution in [O III]  $\lambda 5007$  flux can conservatively be estimated to be  $< 2\%$ .

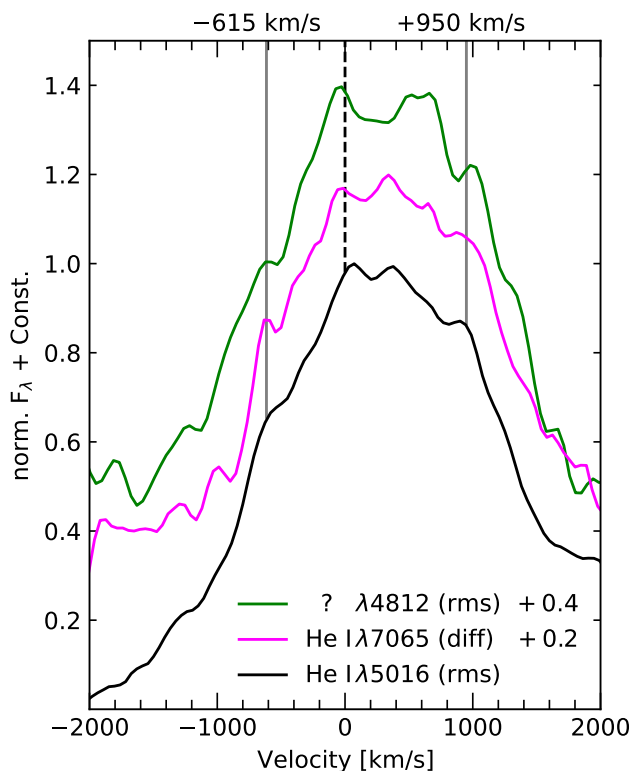


**Fig. 13.** Comparison of the profiles of He I  $\lambda 5016$ , He I  $\lambda 7065$  and the unidentified line species at approximately  $4812 \text{ \AA}$  in velocity space. We subtracted a suitable linear pseudo-continuum from each line and shifted the profiles in flux for clarity. The positions of the left and right peak of Ca II  $\lambda 8662$  at  $-615 \text{ km s}^{-1}$  and  $+950 \text{ km s}^{-1}$ , respectively, are indicated with gray lines. All three line profiles show indications for a similar double-peaked structure and have an identical width of FWHM  $\approx 2170 \text{ km s}^{-1}$  when normalized to the profile peak, and of FWHM  $\approx 2500 \text{ km s}^{-1}$  when the additional central emission is taken into account.

From the MUSE spectra of the nuclear region and the H II region taken on 2015 September 24, we find that the V-band flux in the H II region is 7% of that in the low-state nuclear spectrum. However, this measurement still includes the strong stellar host-contribution, which we estimate to account for  $\sim 70\%$  of the V-band flux (see 3.1.1). This reduces the potential continuum contribution of the H II region to the host-free nuclear spectra to  $\sim 4\%$ . Taking into account the minimal overlap between apertures, this further reduces the contribution to  $< 1\%$  for the MUSE and  $< 2\%$  for the SALT spectra. We conclude that the H II region contributes only insignificantly to the nuclear spectra presented in this paper.

## 4.2. The double-peaked Ca II triplet and O I line profiles

### 4.2.1. Robustness of the double-peaked difference profiles

We show in 3.2.1 that the difference line profile of Ca II  $\lambda 8662$  is “lopsided” and double-peaked, exhibiting a skewed dip in the central profile. It closely resembles line profiles observed in a number of AGN and TDEs (see 3.2.1), which are interpreted to arise in an elliptical accretion disk. To our knowledge, this is the first time “genuine” double-peaked Ca II triplet emission – as well as double-peaked  $L\beta$ -pumped O I  $\lambda 8446$  emission – in AGN has been presented in the literature. Only recently, Dias dos Santos et al. (2023) found, for the first time, a double-peaked

O I  $\lambda 11279$  profile in III Zw 002. Out of the 14 Ca II emitters shown by Persson (1988a), none shows unambiguous indications for a double-peaked profile caused by gas kinematics. Instead, Persson (1988a) attributes the central dips present in some Ca II emitters, such as Mrk 42, to underlying stellar absorption from the host galaxy. However, genuine double-peaked Ca II profiles were detected in spectra of cataclysmic variables and associated with emission from an accretion disk (e.g., Persson 1988b, and references therein).

We omit the effect of Ca II absorption by extracting the Ca II difference line profile between the observations taken on 2015 September 24 and 2017 October 23, respectively. The robustness of the double-peaked profile therefore depends directly on the quality of the intercalibration of these two spectra. The quality of the intercalibration can be directly assessed from Fig. 9. The two spectra we intercalibrated such that the stellar signature of the host galaxy and the narrow lines in the difference profile vanish. The difference spectrum reveals only broad line emission, indicating a successful intercalibration of the two spectra.

The strongest argument for a successful correction for Ca II absorption is provided by comparing the line profile of Ca II  $\lambda 8662$  with that of O I  $\lambda 8446$  and Ca II  $\lambda 8542$ . The blue wing of O I  $\lambda 8446$  is neither influenced by strong absorption nor by blending with Ca II  $\lambda 8498$ . Likewise, the red wing of Ca II  $\lambda 8542$  is free of absorption as well as line blending effects. We show a comparison of the Ca II  $\lambda 8662$  difference line profile with the blue wing of O I  $\lambda 8446$  and the right wing of Ca II  $\lambda 8542$  in Fig. 15. The profiles of O I  $\lambda 8446$  and Ca II  $\lambda 8542$  are normalized to their left and right peak, respectively, and shifted downwards for clarity. All profiles exhibit identical line features, namely a pronounced left peak ①, the same lopsidedness and characteristic small-scale features in the central profile ②, and a triple-peaked red peak ③ that resembles a trident. Although the exact position, width and scaling of the blue peak and the small-scale features in the O I  $\lambda 8446$  profile differ slightly from that in the Ca II  $\lambda 8662$  profile, the qualitative profile is identical. We therefore conclude that the Ca II  $\lambda 8662$  difference line profile presented in Fig. 10 is in fact the clean profile and that residual Ca II absorption is not significantly affecting the line profile. More precisely, the skewed, lopsided profile is exclusively due to the structure and kinematics of the BLR.

### 4.2.2. The elliptical accretion disk model for Ca II $\lambda 8662$

We show in 3.2.2 that the Ca II  $\lambda 8662$  difference profile (and in turn the O I profile and the other Ca II profiles), with exception of the inner part of the profile, is in general well approximated by line emission from a relativistic elliptical accretion disk. In particular, the model reproduces the observed shape of the line wings, and only the red peak of the model fit is marginally shifted inwards by about  $50 \text{ km s}^{-1}$  with respect to the observed profile. This indicates that the structure (and/or kinematics) of the disk generating the line profile might be more complex than a homogeneous elliptical disk, thereby causing the trident structure in the red peak (see 4.4.3 for further details).

The model reproduces a low disk inclination of  $i = (8.10 \pm 3.00)^\circ$  in agreement with findings of Parker et al. (2019), who found  $i < 11^\circ$ , and with the almost face-on view of the host galaxy, though we note that NGC 1566’s host-galaxy geometry is more complex on larger scales (Elagali et al. 2019). The major axis viewing angle, which is the angle between the major axis in apocenter direction and the projected line-of-sight in the disk plane, is  $\phi_0 = (193.29 \pm 26.00)^\circ$ . The disk is confined within the inner and outer pericenter distances  $\xi_1$  and  $\xi_2$  of

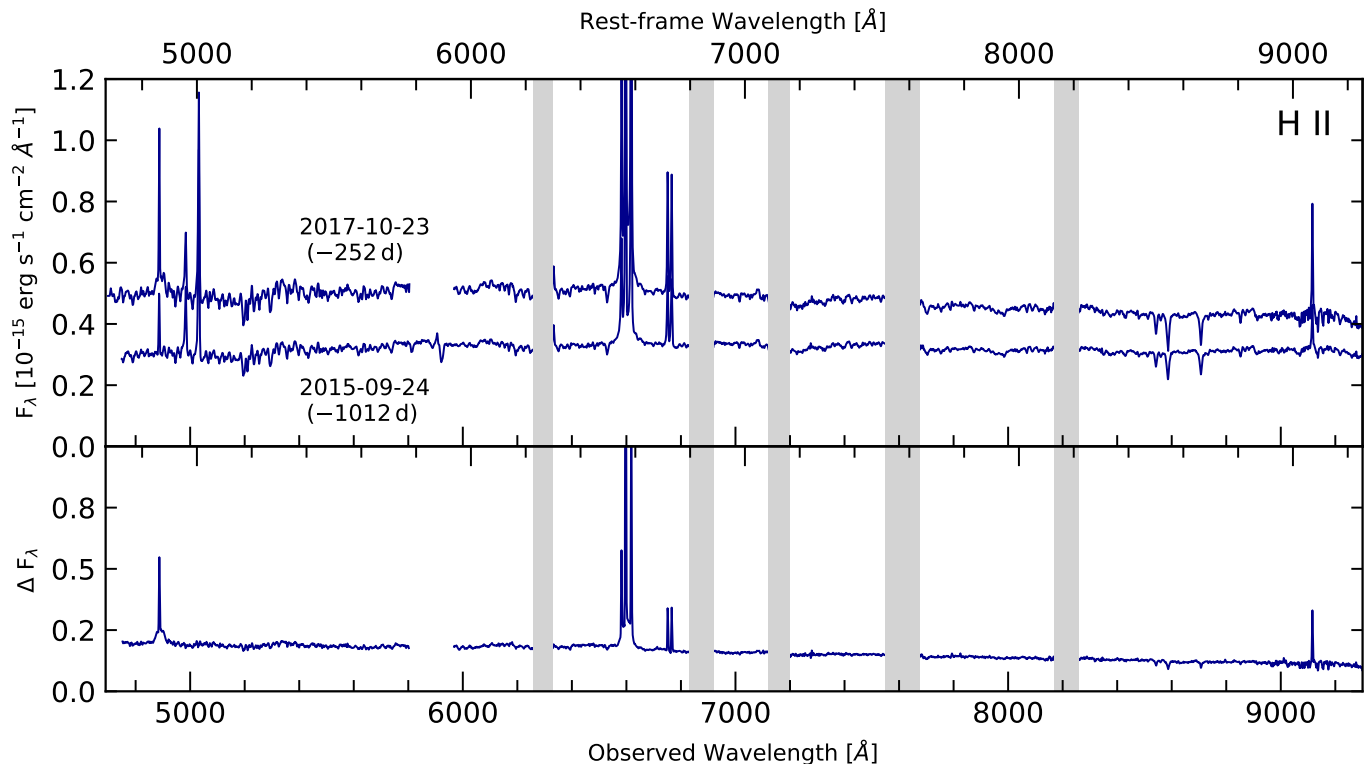


**Fig. 14.** Spectrum of the H II region at a distance of  $\Delta d \sim 1''0$  from the nucleus taken on 2015 September 24 and 2017 October 23, respectively, intercalibrated to the same [O III]  $\lambda 5007$  flux of  $(4.2 \pm 0.3) \times 10^{-15} \text{ ergs s}^{-1} \text{ cm}^{-2}$  (upper panel) and the resulting difference spectrum (lower panel). Spectral regions strongly influenced by telluric absorption are shown in gray. The apparent continuum flux increase on 2017 October 23 is caused by scattered radiation from the brightening nucleus.

$(2231 \pm 1000) r_g$  and  $(4050 \pm 1500) r_g$ , respectively, and exhibits very low internal broadening with  $\sigma = (87 \pm 10) \text{ km s}^{-1}$ . The eccentricity of  $e = 0.57 \pm 0.35$  is moderate, and the emissivity power-law index  $q$  amounts to  $4.34 \pm 0.80$ . This is larger than the value of  $q \approx 3$  for the emissivity profile of an outer accretion disk ( $\geq 100 r_g$ ) irradiated by an isotropic point source (or simple extended source) of X-ray emission (see Wilkins & Fabian 2012, and references therein) usually adopted in other studies (e.g., Eracleous & Halpern 1994, 2003).

Our best-fit model is able to reproduce all key features of the Ca II  $\lambda 8662$  profile, namely the redward asymmetry and the narrow blue and red peak, respectively. It cannot, however, account for all of the emission in the central part of the profile between  $-450 \text{ km s}^{-1} < v < +850 \text{ km s}^{-1}$ . This discrepancy between disk-modeled line profiles and observed line profiles has been noticed in other studies (e.g., Hung et al. 2020; Wevers et al. 2022; Dias dos Santos et al. 2023), and has been attributed to additional emission from gas above the disk plane. In contrast to previous studies, we do not attempt to recover the additional emission component by a Gaussian component as this component in our model is clearly not a Gaussian. Instead, the central emission component has a distorted, rather flat-topped profile with a pronounced redward asymmetry.

In agreement with the aforementioned studies, we attribute this additional emission component to emission from BLR clouds situated above the accretion disk plane, apparently not retaining the angular momentum of the disk. The observed redward asymmetry might be explained by the asymmetric distribution of clouds with respect to the ionizing continuum, which we assume to be in close vicinity to the SMBH. Regardless of the

exact distribution of BLR gas above the disk, we conclude that the BLR in NGC 1566 is a two-component BLR, consisting of a BLR disk component and an additional component of BLR gas above the disk plane.

For a sample of six AGN, Eracleous et al. (1995) found pericenter distances  $\xi_1$  and  $\xi_2$  for H $\alpha$  ranging between  $350 - 1900 r_g$  and  $3000 - 9000 r_g$ , respectively. For a sample of 116 double-peaked Balmer line AGN, Strateva et al. (2003) found the accretion disks to be consistent with inner radii of  $(200 - 800) r_g$ , and outer radii  $\geq 2000 r_g$ . This places our inner pericenter distance  $\xi_1$  at the higher end of the distribution, and the outer pericenter distance  $\xi_2$  at the lower end. Nevertheless, the scatter in the modeled disk extents for different objects is rather large. For example, Ricci & Steiner (2019) found both pericenter distances  $\xi_1$  and  $\xi_2$  for H $\alpha$  in NGC 4958 to be  $< 1000 r_g$ . Storchi-Bergmann et al. (1997) found pericenter distances  $\xi_1$  and  $\xi_2$  of  $1300 r_g$  and  $1600 r_g$  in NGC 1097 using their refined elliptical disk model, indicating a rather ring-like structure.

In order to test the robustness of our solution, we now calculate the expected lag of H $\beta$  using the  $R_{H\beta} - \lambda L_{5100}$  relationship

$$\log \left[ \frac{R}{11t - \text{day}} \right] = K + \beta \log \left[ \frac{\lambda L_{5100}}{10^{44} \text{ ergs}^{-1}} \right], \quad (6)$$

where  $K$  is the origin and  $\beta$  is the slope of the relation. We expect H $\beta$  to be emitted at approximately the same radial distance as Ca II  $\lambda 8662$ , since we can model the H $\beta$  profile as a Ca II  $\lambda 8662$  profile broadened by a Lorentzian function. This is interpreted as the effect of scale-height-dependent turbulence (see 4.4.1), which in turn means that the underlying rotational kinematics of

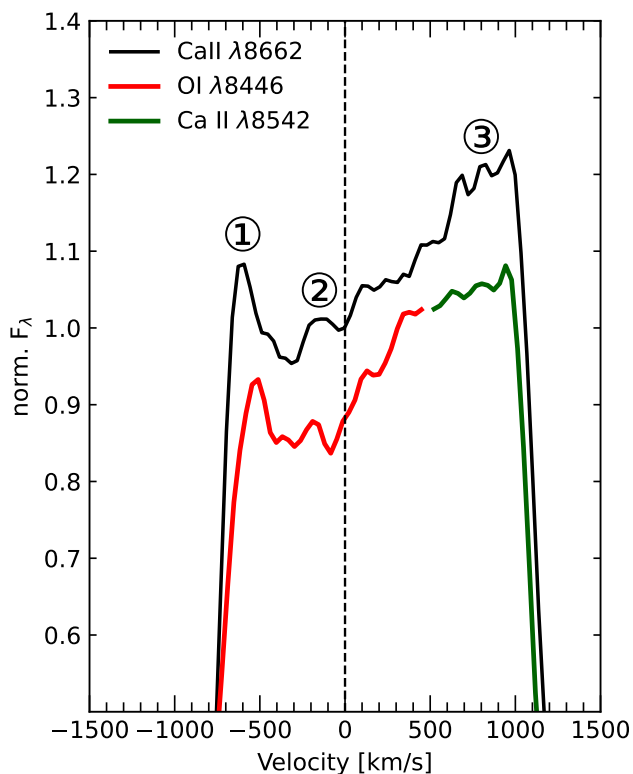


**Fig. 15.** Comparison of the Ca II  $\lambda 8662$  difference line profile (*black*) with the blue wing of O I  $\lambda 8446$  (*red*) and the right wing of Ca II  $\lambda 8542$  (*green*) in velocity space. The profiles of O I  $\lambda 8446$  (*red*) and Ca II  $\lambda 8542$  are normalized to their left and right peak, respectively, and shifted downwards for clarity. All profiles exhibit identical line features, namely a pronounced left peak ①, the same lopsidedness and characteristic small-scale features in the central profile ②, and a triple-peaked (trident) red peak ③.

H $\beta$  and Ca II are identical. Recent works suggest that the FWHM of H $\beta$  and Ca II in high-luminosity sources are tightly correlated, while the FWHM of H $\beta$  in local low-luminosity sources like NGC 1566 is slightly larger than that of Ca II (Martínez-Aldama et al. 2021). We use a slope of  $\beta = 0.53$  as found by Bentz et al. (2013) and Kollatschny et al. (2018),  $K = 1.53$ , and adopt  $\lambda L_{5100} = 3.91 \times 10^{41}$  ergs s $^{-1}$  obtained in 3.1.3. This gives a BLR radius of only  $\sim 1.8$  lt-days. We now compare this value with the delay expected from the best-fit elliptical accretion disk model calculated in 3.2.2. For this purpose, we first calculate the distance  $d = \xi_2/(1-e) - \xi_2$  of the center of the disk to the SMBH using the outer perigee  $\xi_2$  of the disk emitting region and the eccentricity  $e$ . This gives a distance of  $d \approx 5500 r_g$  from the SMBH to the disk center, and with  $M_{\text{BH}} = (5.3 \pm 2.7) \times 10^6 M_{\odot}$  calculated in 3.1.3, which results in a gravitational radius  $r_g = GM/c^2$  of 0.0003 lt-days, we obtain  $\sim 1.7$  lt-days for the expected delay between continuum and line emission in NGC 1566. This is a rough estimate, since the line emission is not weighted by emissivity. Nonetheless, this simple order-of-magnitude assessment confirms that the best-fit disk parameters are in good agreement with established reverberation mapping scaling relations.

#### 4.2.3. The Bowen fluorescence line O I $\lambda 8446$ as part of the elliptical disk model

We find indications for O I  $\lambda 8446$  as well as Ca II triplet emission already being present during the low-state, host-galaxy sub-

tracted spectrum from 2015 September 24 (Spectrum 1; see Fig. 4). Although the S/N of O I and Ca II in the host-galaxy subtracted spectrum is low and the Ca II triplet is still affected by residual absorption, we identify the blue wing of O I  $\lambda 8446$  together with its blue peak. We show a comparison between the blue O I  $\lambda 8446$  wing from 2015 September 24 and the blue O I  $\lambda 8446$  wing from the difference spectrum in Fig. 16. The blue wing of O I  $\lambda 8446$  from the low-state spectrum is scaled and smoothed for clarity. We find a blueward drift of about  $-(150 - 200)$  km s $^{-1}$  with respect to the low-state spectrum. For comparison, H $\beta$  shifted by  $-240$  km s $^{-1}$  between Spectrum 1 and Spectrum 2 (from 2015 September 24 to 2017 October 23). This indicates that O I  $\lambda 8446$  shifts in tandem with the Balmer lines (see 3.1.2), but not necessarily by the exact same amount.<sup>8</sup>

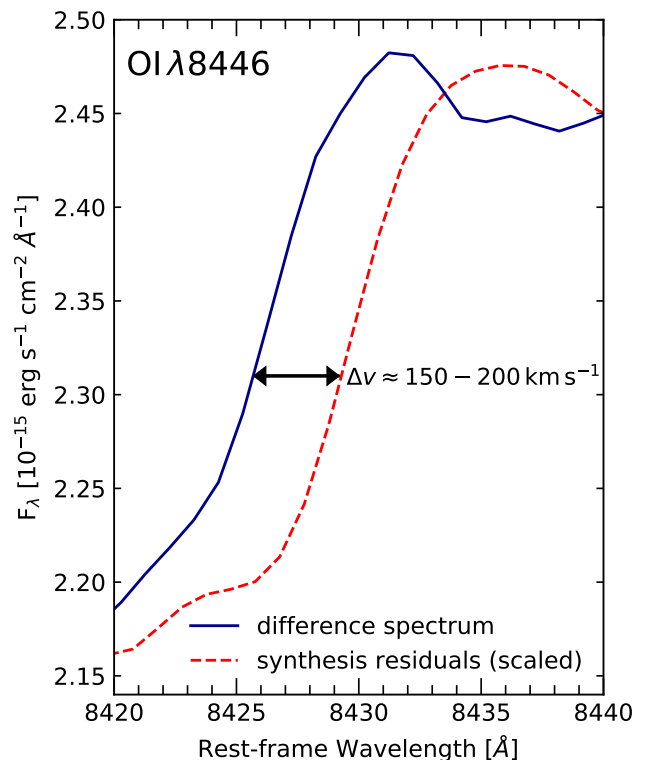


**Fig. 16.** Comparison of the blue wing of O I  $\lambda 8446$  between the difference spectrum from 2015 September 24 to 2017 October 23 (*blue*) and the host-subtracted residuum spectrum from 2015 September 24 (slightly smoothed and scaled for clarity; *red*) resulting from the stellar synthesis in 3.1.1. The shift of the blue wing of O I  $\lambda 8446$  from 2015 September 24 to 2017 October 23 indicates a blueward drift of the line emission. The difference velocity  $\Delta v_{\text{shift}}$  amounts to  $\Delta v_{\text{shift}} \approx 150 - 200$  km s $^{-1}$ .

In the following, we discuss the production channels of O I  $\lambda 8446$  and its region of origin. O I  $\lambda 8446$  emission can be produced by either recombination, collisional excitation by electrons, continuum fluorescence, Ly $\beta$  fluorescence (a process first described by Bowen (1947), hence also termed Bowen fluorescence) or a combination of these mechanisms (for a review see Grandi 1980). The exact mechanism(s) responsible for the emission of O I  $\lambda 8446$  in a particular source can be determined by

<sup>8</sup> We also find apparent blueward drifts of the same order in the red wings of Ca II  $\lambda 8662$  and Ca II  $\lambda 8662$ . However, the S/N in the host-galaxy-subtracted spectrum is too low and the profiles are affected by residual absorption, meaning that no robust quantitative estimate of the shift can be made.



performing line diagnostics with respect to other O I lines in this source. [Rodríguez-Ardila et al. \(2002b\)](#) performed line diagnostics on the O I lines  $\lambda\lambda 1304, 7774, 8446, 11287$  in a sample of six AGN. They found O I  $\lambda 8446$  to be formed through collisional excitation and Ly $\beta$  fluorescence, and excluded recombination and continuum fluorescence as a source of the observed line strength of O I  $\lambda 8446$ . [Matsuoka et al. \(2007\)](#) later corroborated these results by means of photoionization models.

O I  $\lambda 8446$  emission in AGN has been known for several decades, and has early been associated with the broad line region due to the absence of a narrow component ([Grandi 1980](#)). We can confirm the absence of a narrow O I  $\lambda 8446$  component in NGC 1566, and, moreover, report that O I  $\lambda 8446$  and the lines of the NIR Ca II triplet exhibit virtually identical line profiles (see Fig. 15). [Persson \(1988a\)](#) found a tight correlation between the FWHM of O I  $\lambda 8446$  and the Ca II triplet, indicating that the O I and Ca II lines stem from approximately the same region. Likewise, [Rodríguez-Ardila et al. \(2002a\)](#) concluded by virtue of identical line profiles, that O I and Ca II share the same kinematics. We can confirm this result based on the identical line profiles, that place the emitting gas in a region dominated by the kinematics of an elliptical disk (see 4.2.2). We stress, however, that the profile of O I  $\lambda 8446$  exhibits a more redshifted blue peak and a shallower blue wing than Ca II  $\lambda 8662$ . This required convolving the Ca II  $\lambda 8662$  profile with a Gaussian of small width in order to reproduce the slope of the left wing of O I  $\lambda 8446$  when reconstructing the blended O I and Ca II triplet complex. Such a slight change in the profile's shape can be achieved in the best-fit Ca II  $\lambda 8662$  model by increasing the inner pericenter distance  $\xi_1$  by about 10%. We therefore speculate that emission of O I  $\lambda 8446$  takes place in a similar, overlapping region with respect to emission of Ca II, and that this region has a marginally larger inner radius.

Bowen fluorescence lines have recently gained attention by the detection and definition of a new class of transient events in AGN by [Trakhtenbrot et al. \(2019b\)](#). They described a new class of long-lived (a few years) transient events during which broad N III  $\lambda 4640$  (as well as O III  $\lambda 3133$  and N III  $\lambda 4097, 4103$ ; see [Makrygianni et al. 2023](#), and references therein) is generated by the absorption of He II Ly $\alpha$  by O III. O III then de-excites through a series of optical transitions and a far-UV transition at 374.436 Å, which in turn excites N III, generating optical emission of N III  $\lambda\lambda 4097, 4104, 4379, 4634, 4641$  ([Bowen 1928, 1935](#)). We note that Ly $\beta$  pumping, and therefore the generation of O I  $\lambda 8446$ , follows a different production channel, namely the absorption of H I Ly $\beta$  (1025.72, Å) by O I, directly leading to the emission of O I  $\lambda\lambda 1304, 8446, 11287$  through optical de-excitation.

The presence of enhanced ionizing UV emission during Bowen fluorescence flares has been attributed to enhanced accretion onto the SMBH ([Trakhtenbrot et al. 2019b; Makrygianni et al. 2023](#)) in a pre-existing AGN. Based on the detection of weak O I  $\lambda 8446$  emission in NGC 1566 present already before the transient event, we likewise attribute the enhanced UV emission ([Oknyansky et al. 2020](#)) and the in turn enhanced O I  $\lambda 8446$  emission during the event to an increase in accretion rate.

#### 4.2.4. Density and column density in the O I and Ca II disk

Based on the almost identical line profiles of O I  $\lambda 8446$  and Ca II, we show in 4.2.3 that both lines originate from approximately the same region, and that this region is dominated by the kinematics of an elliptical accretion disk. We now show that this is

consistent with photoionization calculations, which indicate that both O I  $\lambda 8446$  and Ca II are emitted from a region of similar (column) density. In 3.2.3, we find a Ca II triplet ratio of 1:1:1 and an O I  $\lambda 8446$ -to-Ca II  $\lambda 8662$  ratio of 0.85:1. The Ca II T : O I  $\lambda 8446$  ratio is therefore 3.5. [Persson \(1988a\)](#) pointed out that if Ca II triplet emission is detected in AGN, the Ca II triplet ratio is usually on the order of 1:1:1. This indicates that the Ca II emission arises from a region that is optically thick in Ca II. Model calculations for Ca II ([Joly 1989; Ferland & Persson 1989](#)) placed the emitting region in a cool and dense gas with a temperature  $T \leq 8000$  K, a density of  $n_H \approx 10^{12} \text{ cm}^{-3}$ , and a column density of  $N_H \geq 10^{23} \text{ cm}^{-2}$ . More recent studies corroborated the results for the gas and column density ([Panda et al. 2020; Panda 2021a,b](#)). These physical conditions are the conditions of an outer, cold accretion disk, and [Ferland & Persson \(1989\)](#) and later [Dultzin-Hacyan et al. \(1999\)](#) associated Ca II emission with a wind (or corona) just above the accretion disk. Based on photoionization model calculations on surveys of intermediate-redshift quasars, [Matsuoka et al. \(2007\)](#) and [Martínez-Aldama et al. \(2015\)](#) suggested that O I  $\lambda 8446$  and the Ca II triplet are emitted from regions with similar physical conditions. In particular, [Matsuoka et al. \(2007\)](#) restricted the density of the O I and Ca II emitting gas to  $n_H \approx 10^{11.5} \text{ cm}^{-3}$ , and based on our measured Ca II T : O I  $\lambda 8446$  ratio of 3.5 in NGC 1566, their model gives a column density of  $N_H \approx 1.2 \times 10^{23} \text{ cm}^{-2}$  (see Fig. 8 in [Matsuoka et al. 2007](#)) for the O I  $\lambda 8446$  emitting region in NGC 1566. In summary, we suggest that O I and Ca II are emitted in a similar, overlapping region, as argued before on basis of the identical line profiles.

#### 4.3. Helium profiles and the unidentified emission at 4812 Å

In 3.3 and 3.4 we identify emission of He I  $\lambda\lambda 4922, 5016, 7065$  based on their identical line profiles. The profiles of He I  $\lambda\lambda 5016, 7065$  show, in comparison to the profiles of O I  $\lambda 8446$ , Ca II  $\lambda\lambda 8498, 8542, 8662$ , and the “smoothed” profile of H $\beta$ , a much stronger central emission component, whereas the double-peak structure is almost completely suppressed. The He I profiles bear a remarkable resemblance to the late-time H $\alpha$  profiles observed in the TDE AT 2018hyz by [Hung et al. \(2020\)](#), when the central additional emission starts to dominate the line profile. [Hung et al. \(2020\)](#) identified the additional emission to be a nondisk Gaussian component related to a BLR that formed by radiatively driven winds. Likewise, the BLR in NGC 1566 can be modeled as a two-component BLR, namely BLR disk and BLR gas above the disk plane, where the BLR component from above the disk contributes more to the He I lines than to the other line species. At the same time, the FWHM of the He I disk-component in NGC 1566 is  $\sim 2500 \text{ km s}^{-1}$  and therefore broader by  $\sim 600 \text{ km s}^{-1}$  and  $\sim 300 \text{ km s}^{-1}$  in comparison to Ca II  $\lambda 8662$  and H $\beta$ , respectively.

The detection of the yet unidentified emission at  $\sim 4812$  Å is based on the striking resemblance between this emission line and the He I  $\lambda\lambda 5016, 7065$  profiles, all of them exhibiting approximately the same width, weak double-peak features and additional strong emission in the central line profile with almost identical small-scale features. The pronounced similarity between the profiles might suggest that this is genuine emission and not just a residual from the reconstruction of H $\beta$  from the double-peaked Ca II profile. If indeed line emission, the exact identification of the line species is difficult, since the central wavelength of  $\sim 4812$  Å is estimated by comparing the line profile with that of He I  $\lambda\lambda 5016, 7065$ . As shown previously, H $\beta$  and O I  $\lambda 8446$  show

significant, but not necessarily identical blueward drifts during the rising phase of the transient event, and we suspect the same to be true for all broad lines. Consequently, we cannot exactly determine the central wavelength of the unidentified emission. Despite the resemblance to the He I profiles, we find the emission at  $\sim 4812 \text{ \AA}$  unlikely to be associated with He I as no emission from He I is expected in a spectral range  $\pm 100 \text{ \AA}$  around this wavelength (see the NIST Atomic Spectra Database<sup>9</sup>).

Véron et al. (2002) associated the “red shelf” observed in some Seyfert 1s (Meyers & Peterson 1985) with broad emission from He I  $\lambda 4922$  and He I  $\lambda 5016$ . We confirm the presence of He I  $\lambda 4922$ , 5016 in NGC 1566 and that they constitute the red shelf of H $\beta$  clearly discernible in the rms spectrum close to H $\beta$  (see Fig. 12). Although the blue wing of He I  $\lambda 4922$  is slightly disturbed by either interference from small H $\beta$  residuals or unidentified line emission, the red wing shows the same shape as the other He I lines. We also find indications for the red wing of He I  $\lambda 4713$ , however, this line is heavily blended with He II  $\lambda 4686$ . The spectral region between  $\sim 4500 \text{ \AA}$  and  $\sim 5600 \text{ \AA}$  in AGN can be densely populated by line emission of Fe II, and previous studies found tight correlations between the properties of Ca II and Fe II emitting regions (Panda et al. 2020; Panda 2021a,b). In particular, Ca II and Fe II are expected to be emitted from gas with the same temperature, density, column density, and their line profile widths indicate an origin from approximately the same spatial region (Marinello et al. 2016, 2020). Hence, since NGC 1566 shows strong Ca II emission, significant optical Fe II emission is expected. Indeed, we observe strong line emission between  $\sim 4500 \text{ \AA}$  and  $\sim 5600 \text{ \AA}$  during the transient event, requiring a careful decomposition and fitting in order to determine the different line contributions. This is, however, beyond the scope of this paper.

#### 4.4. Broad-line region structure and kinematics

##### 4.4.1. The role of turbulence and stratification in the BLR

Spectrum 1 (2015 September 24) and Spectrum 2 (2017 October 23) exhibit very similar H $\beta$  line profiles, and we show in 3.3 that the low-state H $\beta$  profile is in perfect agreement with a double-peaked Ca II  $\lambda 8662$  profile smoothed by a Lorentzian of half width  $\Gamma = 450 \text{ km s}^{-1}$ . The resulting profile itself is not a Lorentzian profile, but is asymmetrical and slightly skewed due to the underlying double-peaked profile. Likewise, we can model the rms profiles of H $\beta$  and H $\alpha$  by exactly the same procedure.<sup>10</sup> This indicates that underlying kinematics do not change drastically during the transient event. We draw two major conclusions from these results: First, since the low-state H $\beta$  profile before the transient event is evidently shaped by the same elliptical-disk kinematics as Ca II  $\lambda 8662$ , the disk-like BLR was already present before the transient event began in 2017. Second, the H $\beta$  profile is influenced by some physical process effectively smearing out the profile with respect to the double-peaked Ca II  $\lambda$  profile. In the following, we show that this smearing of the profile can be attributed to turbulence.

Kollatschny & Zetzl (2013a) and Kollatschny & Zetzl (2013b) were able to parameterize broad emission lines in AGN by the ratio of FWHM to line dispersion  $\sigma_{\text{line}}$ , and modeled line profiles shaped by scale-height-dependent turbulence as

Lorentzian profiles. They obtained distances  $R$  of the line emitting region using reverberation mapping and modeled the scale height  $H$  according to

$$H/R = (1/\alpha)(v_{\text{turb}}/v_{\text{rot}}), \quad (7)$$

given by Pringle (1981), where  $\alpha$  is the viscosity parameter of order unity. The velocities give the turbulent and rotational velocities, respectively. Kollatschny & Zetzl (2013a) and Kollatschny & Zetzl (2013b) found a flattened distribution for the H $\beta$  emitting region, and in particular that the height of the line emitting region increases with distance to the SMBH, resulting in a flat bowl-shaped geometry. Strikingly, Kollatschny & Zetzl (2013a) found for a large sample of AGN that each emission line was associated with a specific turbulent velocity, and in particular that the turbulent component in H $\beta$  profiles corresponded to turbulent motions of  $v_{\text{turb}} \sim 400 \text{ km s}^{-1}$ . Goad et al. (2012) found that Lorentzian profiles of the emission lines naturally arise for low-inclination systems in their bowl-shaped BLR model, and evidence for bowl-shaped BLR geometries (e.g., Ramolla et al. 2018, and references therein) or in general flattened or disk-like geometries (e.g., Gaskell et al. 2007; Pancoast et al. 2014; Williams et al. 2018) have also been found by other studies.

As the temporal sampling of the presented variability campaign of NGC 1566 during the transient event is too low to perform classical reverberation mapping, we are not able to obtain geometrical information from the transfer function. Therefore, we cannot make a precise prediction about the exact shape of the BLR; that is, whether it is rather disk-like or bowl-shaped. However, as the aforementioned models associate turbulence with scale height above the disk, we deduce a vertical stratification of the BLR; that is, H $\beta$  is emitted at greater scale height than Ca II and O I: For  $\alpha$  set to 1, the turbulent velocities  $v(\text{Ca II})_{\text{turb}} = 200 \text{ km s}^{-1}$  (see 4.2.2) and  $v(\text{H}\beta)_{\text{turb}} = 900 \text{ km s}^{-1}$  as well as  $\text{FWHM}(\text{Ca II}) = 1920 \text{ km s}^{-1}$  and  $\text{FWHM}(\text{H}\beta) = 2200 \text{ km s}^{-1}$ , we obtain an  $H/R$  value of  $\sim 0.1$  and  $\sim 0.4$  for Ca II and H $\beta$ , respectively. Therefore, H $\beta$  is being emitted roughly at four times the height of Ca II.

Although the He I profiles do not allow for a reliable fit with the elliptical disk model alone, we note that we can in principle construct such “smeared out” broader profiles (in comparison to H $\beta$ ) by decreasing the inner and outer pericenter distance of the emitting region while at the same time increasing the internal broadening. This indicates that the He I emission is generated at shorter distances from the ionizing continuum (“further in”), paired with higher internal broadening, which can be interpreted as turbulence due to greater scale height and therefore a higher layer in the disk. This is in agreement with results of Kollatschny & Zetzl (2013b), who showed that high-ionization lines are emitted closer to the SMBH, but at greater heights.

In conclusion, we term the BLR in NGC 1566 to be *disk-dominated*. This means that all broad emission lines analyzed in this study (H $\beta$ , He I, Ca II, and O I) show the kinematic signature of an elliptical accretion disk. While this signature is clearly visible in the line profiles of Ca II, and O I as they are being emitted closest to the midplane of the disk, it is smeared out by turbulence (and in some part by the presence of additional emission components) in the case of H $\beta$  and He I.

##### 4.4.2. Temporal evolution of the Balmer profiles: A possible disk wind.

We show in 3.1.2 and 4.2.3, that H $\beta$  and O I  $\lambda 8446$  exhibit blueward drifts by  $-240 \text{ km s}^{-1}$  and  $-(150 - 200) \text{ km s}^{-1}$ , respectively, during the rising phase of the transient event (between

<sup>9</sup> [https://physics.nist.gov/PhysRefData/ASD/lines\\_form.html](https://physics.nist.gov/PhysRefData/ASD/lines_form.html)

<sup>10</sup> We note that the rms spectrum is dominated by the two strongest spectra closest to the transient peak.

Spectrum 1 and Spectrum 2). When fitting line profiles with accretion disk models, velocity shifts due to other physical processes affect the (a)symmetry of the profile and may prevent the determination of the true disk parameters if not taken into account. This problem regarding velocity shifted line profiles has already been addressed by [Eracleous et al. \(1995\)](#) and [Eracleous & Halpern \(2003\)](#) with respect to possible orbital motions in a binary system used to explain the formation of eccentric disks. In the following, we investigate the impact of the blueward drift on the best-fit parameter set and discuss possible explanations for the observed line profile shifts.

Supposing that Ca II exhibits a velocity shift similar to O I  $\lambda 8446$ , and that the line profile does not change significantly (as indicated by the almost identical H $\beta$  profiles during the onset of the transient event), we perform a fit on a Ca II  $\lambda 8662$  profile that we artificially redshift by  $+200 \text{ km s}^{-1}$ . This way, we compensate the blueward drift of the line during the transient event and obtain, presumably, the original Ca II  $\lambda 8662$  before the transient event. We find that we are able to fit the shifted Ca II  $\lambda 8662$  profile with the disk parameters  $\xi_1 = (1140 \pm 800) r_g$ ,  $\xi_2 = (4468 \pm 1600) r_g$ ,  $i = (5.64 \pm 3.00)^\circ$ ,  $\phi_0 = (207.94 \pm 26.00)^\circ$ ,  $\sigma = (85 \pm 10) \text{ km s}^{-1}$ ,  $e = (0.55 \pm 0.40)$ , and  $q = (4.50 \pm 0.90)$ . This fit largely reproduces the best-fit parameters obtained in 3.2.2 within their error margins, except for the inner pericenter distance  $\xi_1$ , which decreased by half and is now slightly below the determined margin of error.

We now discuss the blueward drift of the H $\beta$  profile in the context of line profiles presented in previous studies. The H $\beta$  profile shifted by  $-240 \text{ km s}^{-1}$  within  $\sim 750$  days (between Spectrum 1 and Spectrum 2) and by additional  $-130 \text{ km s}^{-1}$  within the next 270 days (between Spectrum 2 and Spectrum 3; see Fig. 8). However, previous low-state observations over the last 30 years indicate a constant redshift of the H $\beta$  line. [Kriss et al. \(1991\)](#) found an H $\beta_{\text{broad}}$  velocity shift of  $\sim +700 \text{ km s}^{-1}$  in their HST/FOS spectrum from 1991. Likewise, we find an H $\beta$  redshift of  $(+670 \pm 50) \text{ km s}^{-1}$  in the mean spectrum of a variability campaign on NGC 1566 we performed from 2012 November to 2013 March from which we presented a spectrum in [Oehmann et al. \(2020\)](#). A velocity shift of  $(+375 \pm 6) \text{ km s}^{-1}$  in a GMOS spectrum obtained in 2013 October was reported by [da Silva et al. \(2017\)](#). However, their analysis is primarily based on H $\alpha$  due to its preferable S/N, and the Gaussian fit to H $\beta_{\text{broad}}$  does not capture the line profile of H $\beta$  well. As the H $\beta$  profile from [da Silva et al. \(2017\)](#) and the line profile from our 2012 to 2013 campaign are, by visual inspection, virtually identical, we conclude that the velocity shift in the GMOS spectrum from 2013 October is in fact closer to  $\sim +700 \text{ km s}^{-1}$ . The stability of the H $\beta$  (and H $\alpha$ ) profile was already pointed out by [Alloin et al. \(1985\)](#), who noticed that no considerable changes in the shape of the broad components were present, despite ample changes in total flux during their observations lasting from 1980 to 1982.

Given the stability of the line profile on timescales of years, the consistent velocity shift of  $\sim +700 \text{ km s}^{-1}$  for H $\beta_{\text{broad}}$  over the last 30 years, and indications for slightly different velocity shifts in H $\beta$  and O I  $\lambda 8446$ , a disk wind might serve as an intuitive explanation for the observed blueward drift of the H $\beta$  profile. Accretion disk winds are thought to play an important role in the formation of the BLR ([Czerny & Hryniewicz 2011](#)), and they have been invoked to explain several observational key features of the BLR, for example, the lower redshifts of low-ionization broad emission lines (BELs) in comparison to high-ionization BELs ([Gaskell 1982](#)), or the broad absorption lines (BALs) seen in the UV spectra of some AGN ([Weymann et al. 1991](#)). [Gaskell \(1982\)](#) tied the different redshifts be-

tween low- and high-ionization BELs to two different ionization zones, and it was later suggested that these zones are the low-ionization surface layer of a high-density accretion disk and a high-ionization, low-density wind launched from the accretion disk ([Collin-Souffrin 1987](#); [Collin-Souffrin et al. 1988](#), and references therein). Generally, accretion disk winds can have a severe impact on the observed line profile shapes, in particular depending on the optical depth of the wind (e.g., [Chiang & Murray 1996](#); [Murray & Chiang 1997](#); [Flohic et al. 2012](#)). If the optical depth is low, accretion disk winds can induce blueshifts on lines without changing their profiles ([Eracleous & Halpern 2003](#)). A disk wind would be consistent with results from [Parker et al. \(2019\)](#), who found indications for a  $v \sim 500 \text{ km s}^{-1}$  outflow being launched during the outburst in NGC 1566. On basis of the results presented in this paper, namely the blueward drift of the line profiles and differing velocity shifts between individual lines, we propose a launching accretion disk wind as an explanation for the blueward drift of H $\beta$  and O I  $\lambda 8446$  during the rising phase of the transient event in NGC 1566.

We note that changes in the line profiles caused by accretion disk winds might explain the more complex H $\beta$  profiles observed in later stages of the transient event (see Fig. 7), when NGC 1566 transitions from a Sy 1.2 back to a Sy 1.8 galaxy ([Elitzur et al. 2014](#)).

#### 4.4.3. Evidence for BLR (and AD) inhomogeneities

We show in 4.2.1 that the small-scale features in the O I and Ca II line profiles are not caused by absorption or blending effects, but are genuine features of the double-peaked profiles. The homogeneous elliptical disk model applied in 3.2.2 is not able to account for these features, and the small-scale variations in the profile remain imprinted on the residual flux. The most prominent deviation from the elliptical-disk profile is the trident structure in the red peak, that appears to be constituted by three individual, overlapping peaks. This might, for example, indicate that the inner orbit of the BLR disk in NGC 1566 is in fact split, such that the high-velocity part of the profile splits up. Although our current modeling cannot distinguish if the small-scale line features in the two-component BLR model originate from the disk or the gas above the disk plane, the trident in the red peak makes it intriguing to associate the small-scale deviations with inhomogeneities in the BLR disk structure, which we argue to be tightly connected to an underlying accretion flow. Inhomogeneities appear to be a key feature in AGN accretion disks (e.g. [Dexter & Agol 2011](#); [Jiang & Blaes 2020](#)), and are, for example, invoked to explain the variability in AGN. Inhomogeneities in the BLR have been invoked in the literature in the past to explain broad-line profile changes (e.g., [Veilleux & Zheng 1991](#); [Wanders 1995](#)) on timescales of years, and more recently [Horne et al. \(2021\)](#) identified azimuthal structures rotating in the BLR of NGC 5548, revealing that the BLR is not a homogeneous entity. Structural BLR models incorporating inhomogeneities in the BLR invoke, among others, spiral arms or hot spots in the disk (e.g., [Gilbert et al. 1999](#); [Storchi-Bergmann et al. 2003](#); [Jovanović et al. 2010](#)) and spiral arm models are able to explain the generally observed differences between average and rms profiles as well as complex subfeatures in velocity-delay maps ([Wang et al. 2022](#); [Du & Wang 2023](#)). The detection of BLR inhomogeneities in the profiles of O I and Ca II in NGC 1566 suggests that reverberation mapping of these lines could be a powerful instrument to investigate the BLR structure in AGN in more detail. This has already been noted by [Matsuoka et al. \(2008\)](#).

#### 4.4.4. A turbulent and disk-dominated BLR model as an explanation for the observed emission line profiles

We show above that the line profiles in NGC 1566 during the transient event are shaped by the superposition of at least three effects: (1) The asymmetric and double-peaked O I and Ca II profiles can be modeled by an elliptical, eccentric disk component; (2) the H $\beta$  line profiles can be modeled as broadened versions of these profiles, a fact that we ascribe to scale-height-dependent turbulence; and (3) the line profiles exhibit blueward drifts during the rising phase of the transient event, a circumstance that might be interpreted as the signature of a low-optical-depth disk wind being launched during the transient event. In the emerging BLR picture, the BLR is not only radially stratified with regard to its ionization structure, but also vertically stratified with regard to scale-height-dependent turbulence. Based on the larger FWHM of the He I lines in comparison to H $\beta$ , O I, and Ca II, He I is presumably emitted at shorter radial distance from the ionizing source than the other lines. Furthermore, according to our model H $\beta$  is emitted at greater scale height than O I, and Ca II, but roughly at the same radial distance. To illustrate, we show a qualitative sketch of our BLR model in Fig. 17.

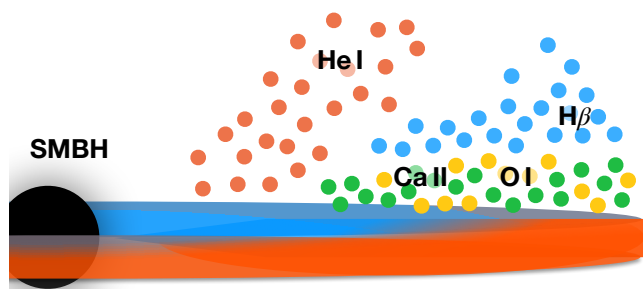


**Fig. 17.** Qualitative edge-on view of the BLR geometry suggested for NGC 1566 (not to scale and the height of the BLR above the disk plane is largely exaggerated for clarity). The blue and red color of the disk vaguely represents the transition from a hotter inner to a cooler outer accretion disk. The BLR has a flattened distribution, with O I and Ca II being emitted close to the midplane of the accretion disk. H $\beta$  is emitted at greater scale height. He I is emitted at shorter radial distance from the ionizing source.

## 5. Conclusions

In this study, we present results of a spectroscopic variability campaign performed on NGC 1566 during its transient event from 2017 to 2019. In particular, we analyzed the emission line profiles of Ca II, O I, He I, H $\beta$ , and H $\alpha$ , and the corresponding profile changes during the event. Our results can be summarized as follows:

1. NGC 1566 exhibits strong spectral changes during its transient event from 2017 to 2019. We observe the emergence and subsequent fading of a strong, power-law-like blue continuum as well as the brightening and subsequent fading of strong Balmer, He I, and He II lines. In addition, we observe

variable coronal line emission of [Fe VII], [Fe X], and [Fe XI]. Further, more detailed results on the spectral variability in NGC 1566 during its transient event will be presented in future publications.

2. We report the detection of double-peaked profiles of the Bowen-fluorescence line O I  $\lambda$ 8446 and Ca II with redward asymmetry during the transient event. To our knowledge, this is the first time that genuine double-peaked O I  $\lambda$ 8446 and Ca II triplet emission line profiles in AGN have been presented in the literature. Moreover, we find indications that O I  $\lambda$ 8446 as well as NIR Ca II triplet emission was already present before the onset of the transient event. The O I  $\lambda$ 8446 and Ca II triplet emission line profiles are well approximated by a combination of emission from an eccentric disk with a low inclination angle of  $i = (8.10 \pm 3.00)^\circ$  and an emission component from BLR gas above the disk. In addition, we interpret small-scale features in the Ca II line profile as evidence for inhomogeneities in the broad-line region associated with the accretion disk.
3. We find a NIR Ca II triplet ratio of 1:1:1 and an O I  $\lambda$ 8446-to-Ca II  $\lambda$ 8662 ratio of 0.85:1. Based on the results of previous studies by other authors, this suggests that the emission of O I and Ca II originates from approximately the same region, namely a region of high (column) density with the kinematic signature of a rotating disk.
4. Based on the stable line profiles and the constant FWHM of H $\beta$  during the event, and  $L\beta$ -pumped O I  $\lambda$ 8446 emission already being present before the brightening in NGC 1566, we conclude that the broad-line region associated with the disk was already present before the beginning of the transient event. More specifically, we postulate that the elliptical disk and the associated broad-line region were not formed during the transient event, but were present before the event began.
5. We show that the Balmer line profiles in NGC 1566 exhibit the same redward asymmetry as the O I and Ca II lines, and that, in comparison, they have a slightly larger FWHM. We are able to reconstruct the H $\beta$  and H $\alpha$  rms profiles by convolving the double-peaked Ca II  $\lambda$ 8662 profile with a Lorentzian with a width of  $\sim 900 \text{ km s}^{-1}$ . We suggest that this might be interpreted as broadening due to turbulent motions of the Balmer-line-emitting gas and that this turbulence smears out the double-peaked profile. According to this interpretation, the region of Balmer line emission in the broad-line region is most likely situated at greater scale height above the accretion disk than the region emitting Ca II.
6. We find indications for a blueward drift of the total H $\beta$  and O I  $\lambda$ 8446 profiles during the rising phase of the transient event. These varying velocity shifts might be interpreted as the emergence of a low-optical-depth wind being launched during the transient event. Except for this launching disk wind, the observed kinematics of the BLR remain largely unchanged during the transient event.

Our results suggest a flattened (disk-dominated) broad-line region geometry, with a vertical stratification due to winds in combination with turbulence. Our results demonstrate the usefulness of spectroscopic transient variability campaigns with high data quality, even when sampling is sparse. We especially point out the usefulness of observations of O I  $\lambda$ 8446 and the NIR Ca II triplet, which is due to the close proximity of their emission region to the accretion disk. Further, more densely sampled spectroscopic observations of transient events are strongly desired.

*Acknowledgements.* The authors thank the anonymous referee for detailed and useful comments, which contributed significantly to the improvement of the

manuscript. Furthermore, the authors thank Peter M. Weibacher for helpful discussions regarding the MUSE reduction pipeline, Dragana Ilić for enlightening discussions about emission lines in optical spectra, Paul I. Schwarz for computational advice as well as helpful discussions, and Björn Müller for discussions regarding mathematical details of the fit to the Ca II profile. The authors greatly acknowledge support by the DFG grants KO 857/35-1 and CH 71/34-3. MWO gratefully acknowledges the support of the German Aerospace Center (DLR) within the framework of the “Verbundforschung Astronomie und Astrophysik” through grant 50OR2305 with funds from the German Federal Ministry for Economic Affairs and Climate Action (BMWK). ERC acknowledges support from the National Research Foundation of South Africa. Five spectra reported in this paper were obtained with the Southern African Large Telescope (SALT under proposal codes 2018-1-DDT-004, 2018-1-DDT-008 (PI: Kollatschny) and 2018-2-LSP-001 (PI: Buckley). In addition, this paper is based on observations made with ESO Telescopes at the La Silla Paranal Observatory under programme IDs 096.D-0263 and 0100.B-0116, obtained from the ESO Science Archive Facility.

## References

- Alloin, D., Pelat, D., Phillips, M., & Whittle, M. 1985, *ApJ*, 288, 205
- Alloin, D., Pelat, D., Phillips, M. M., Fosbury, R. A. E., & Freeman, K. 1986, *ApJ*, 308, 23
- Antonucci, R. 1993, *ARA&A*, 31, 473
- Bacon, R., Accardo, M., Adjali, L., et al. 2010, in *Ground-based and Airborne Instrumentation for Astronomy III*, ed. I. S. McLean, S. K. Ramsay, & H. Takami, Vol. 7735, International Society for Optics and Photonics (SPIE), 131 – 139
- Bacon, R., Vernet, J., Borisova, E., et al. 2014, *The Messenger*, 157, 13
- Baldwin, J., Ferland, G., Korista, K., & Verner, D. 1995, *ApJ*, 455, L119
- Bentz, M. C., Denney, K. D., Grier, C. J., et al. 2013, *ApJ*, 767, 149
- Blandford, R. D. & McKee, C. F. 1982, *ApJ*, 255, 419
- Bon, E., Marziani, P., & Bon, N. 2017, in *New Frontiers in Black Hole Astrophysics*, ed. A. Gomboc, Vol. 324, 176–179
- Bowen, I. S. 1928, *ApJ*, 67, 1
- Bowen, I. S. 1935, *ApJ*, 81, 1
- Bowen, I. S. 1947, *PASP*, 59, 196
- Buckley, D. A. H., Swart, G. P., & Meiring, J. G. 2006, in *Society of Photo-Optical Instrumentation Engineers (SPIE) Conference Series*, Vol. 6267, Society of Photo-Optical Instrumentation Engineers (SPIE) Conference Series, ed. L. M. Stepp, 62670Z
- Cappellari, M. 2017, *MNRAS*, 466, 798
- Cappellari, M. & Emsellem, E. 2004, *PASP*, 116, 138
- Cardelli, J. A., Clayton, G. C., & Mathis, J. S. 1989, *ApJ*, 345, 245
- Chiang, J. & Murray, N. 1996, *ApJ*, 466, 704
- Collin-Souffrin, S. 1987, *A&A*, 179, 60
- Collin-Souffrin, S., Alloin, D., & Andriolat, Y. 1973, *A&A*, 22, 343
- Collin-Souffrin, S., Dyson, J. E., McDowell, J. C., & Perry, J. J. 1988, *MNRAS*, 232, 539
- Czerny, B. & Hryniewicz, K. 2011, *A&A*, 525, L8
- da Silva, P., Steiner, J. E., & Menezes, R. B. 2017, *MNRAS*, 470, 3850
- Dai, X., Stanek, K. Z., Kochanek, C. S., Shappee, B. J., & ASAS-SN Collaboration. 2018, *The Astronomer’s Telegram*, 11893, 1
- De Rosa, G., Fausnaugh, M. M., Grier, C. J., et al. 2018, *ApJ*, 866, 133
- Denney, K. D., De Rosa, G., Croxall, K., et al. 2014, *ApJ*, 796, 134
- Dexter, J. & Agol, E. 2011, *ApJ*, 727, L24
- Dexter, J. & Begelman, M. C. 2019, *MNRAS*, 483, L17
- Dias dos Santos, D., Rodríguez-Ardila, A., Panda, S., & Marinello, M. 2023, *ApJ*, 953, L3
- Du, P. & Wang, J.-M. 2023, *A&A*, 671, A26
- Ducci, L., Siebert, T., Diehl, R., et al. 2018, *The Astronomer’s Telegram*, 11754, 1
- Dultzin-Hacyan, D., Taniguchi, Y., & Uranga, L. 1999, in *Astronomical Society of the Pacific Conference Series*, Vol. 175, Structure and Kinematics of Quasar Broad Line Regions, ed. C. M. Gaskell, W. N. Brandt, M. Dietrich, D. Dultzin-Hacyan, & M. Eracleous, 303
- Elagali, A., Staveley-Smith, L., Rhee, J., et al. 2019, *MNRAS*, 487, 2797
- Elitzur, M., Ho, L. C., & Trump, J. R. 2014, *MNRAS*, 438, 3340
- Eracleous, M. & Halpern, J. P. 1994, *ApJS*, 90, 1
- Eracleous, M. & Halpern, J. P. 2003, *ApJ*, 599, 886
- Eracleous, M., Livio, M., Halpern, J. P., & Storchi-Bergmann, T. 1995, *ApJ*, 438, 610
- Ferland, G. J. & Persson, S. E. 1989, *ApJ*, 347, 656
- Flohic, H. M. L. G., Eracleous, M., & Bogdanović, T. 2012, *ApJ*, 753, 133
- Gaskell, C. M. 1982, *ApJ*, 263, 79
- Gaskell, C. M., Bartel, K., Deffner, J. N., & Xia, I. 2021, *MNRAS*, 508, 6077
- Gaskell, C. M., Klimek, E. S., & Nazarova, L. S. 2007, *arXiv e-prints*, arXiv:0711.1025
- Gezari, S., Halpern, J. P., & Eracleous, M. 2007, *ApJS*, 169, 187
- Gilbert, A. M., Eracleous, M., Filippenko, A. V., & Halpern, J. P. 1999, in *Astronomical Society of the Pacific Conference Series*, Vol. 175, Structure and Kinematics of Quasar Broad Line Regions, ed. C. M. Gaskell, W. N. Brandt, M. Dietrich, D. Dultzin-Hacyan, & M. Eracleous, 189
- Goad, M. & Wanders, I. 1996, *ApJ*, 469, 113
- Goad, M. R., Korista, K. T., & Ruff, A. J. 2012, *MNRAS*, 426, 3086
- Graham, M. J., Ross, N. P., Stern, D., et al. 2020, *MNRAS*, 491, 4925
- Grandi, S. A. 1980, *ApJ*, 238, 10
- Green, P. J., Pulgarin-Duque, L., Anderson, S. F., et al. 2022, *ApJ*, 933, 180
- Guainazzi, M. 2002, *MNRAS*, 329, L13
- Guérou, A., Krajnović, D., Epinat, B., et al. 2017, *A&A*, 608, A5
- Horne, K., De Rosa, G., Peterson, B. M., et al. 2021, *ApJ*, 907, 76
- Hu, C., Li, Y.-R., Du, P., et al. 2020, *ApJ*, 890, 71
- Hung, T., Foley, R. J., Ramirez-Ruiz, E., et al. 2020, *ApJ*, 903, 31
- Jayasinghe, T., Stanek, K. Z., Kochanek, C. S., et al. 2019, *MNRAS*, 485, 961
- Jiang, Y.-F. & Blaes, O. 2020, *ApJ*, 900, 25
- Joly, M. 1989, *A&A*, 208, 47
- Jovanović, P., Popović, L. Č., Stalevski, M., & Shapovalova, A. I. 2010, *ApJ*, 718, 168
- Khachikian, E. Y. & Weedman, D. W. 1974, *ApJ*, 192, 581
- Kobulnicky, H. A., Nordsieck, K. H., Burgh, E. B., et al. 2003, in *Society of Photo-Optical Instrumentation Engineers (SPIE) Conference Series*, Vol. 4841, Instrument Design and Performance for Optical/Infrared Ground-based Telescopes, ed. M. Iye & A. F. M. Moorwood, 1634–1644
- Kochanek, C. S., Shappee, B. J., Stanek, K. Z., et al. 2017, *PASP*, 129, 104502
- Kollatschny, W. & Fricke, K. J. 1985, *A&A*, 146, L11
- Kollatschny, W., Grupe, D., Parker, M. L., et al. 2023, *A&A*, 670, A103
- Kollatschny, W., Ochmann, M. W., Zetzl, M., et al. 2018, *A&A*, 619, A168
- Kollatschny, W. & Zetzl, M. 2011, *Nature*, 470, 366
- Kollatschny, W. & Zetzl, M. 2013a, *A&A*, 549, A100
- Kollatschny, W. & Zetzl, M. 2013b, *A&A*, 558, A26
- Komossa, S. & Grupe, D. 2023, *Astronomische Nachrichten*, 344, e20230015
- Kriss, G. A., Hartig, G. F., Armus, L., et al. 1991, *ApJ*, 377, L13
- Landt, H., Bentz, M. C., Ward, M. J., et al. 2008, *ApJS*, 174, 282
- Lawrence, A. 2018, *Nature Astronomy*, 2, 102
- Lewis, K. T., Eracleous, M., & Storchi-Bergmann, T. 2010, *ApJS*, 187, 416
- Liu, F. K., Zhou, Z. Q., Cao, R., Ho, L. C., & Komossa, S. 2017, *MNRAS*, 472, L99
- MacLeod, C. L., Ross, N. P., Lawrence, A., et al. 2016, *MNRAS*, 457, 389
- Makrygianni, L., Trakhtenbrot, B., Arcavi, I., et al. 2023, *ApJ*, 953, 32
- Marinello, M., Rodríguez-Ardila, A., Garcia-Rissmann, A., Sigut, T. A. A., & Pradhan, A. K. 2016, *ApJ*, 820, 116
- Marinello, M., Rodríguez-Ardila, A., Marziani, P., Sigut, A., & Pradhan, A. 2020, *MNRAS*, 494, 4187
- Martínez-Aldama, M. L., Dultzin, D., Marziani, P., et al. 2015, *ApJS*, 217, 3
- Martínez-Aldama, M. L., Panda, S., Czerny, B., et al. 2021, *ApJ*, 918, 29
- Matsuoka, Y., Kawara, K., & Oyabu, S. 2008, *ApJ*, 673, 62
- Matsuoka, Y., Oyabu, S., Tsuzuki, Y., & Kawara, K. 2007, *ApJ*, 663, 781
- Matt, G., Guainazzi, M., & Maiolino, R. 2003, *MNRAS*, 342, 422
- Meyers, K. A. & Peterson, B. M. 1985, *PASP*, 97, 734
- Murray, N. & Chiang, J. 1997, *ApJ*, 474, 91
- Nicastro, F., Martocchia, A., & Matt, G. 2003, *ApJ*, 589, L13
- Noda, H. & Done, C. 2018, *MNRAS*, 480, 3898
- Ochmann, M. W., Kollatschny, W., & Zetzl, M. 2020, *Contributions of the Astronomical Observatory Skalnaté Pleso*, 50, 318
- Oknyansky, V. L., Winkler, H., Tsygankov, S. S., et al. 2020, *MNRAS*, 498, 718
- Oknyansky, V. L., Winkler, H., Tsygankov, S. S., et al. 2019, *MNRAS*, 483, 558
- Onken, C. A., Ferrarese, L., Merritt, D., et al. 2004, *ApJ*, 615, 645
- Osterbrock, D. E. 1977, *ApJ*, 215, 733
- Osterbrock, D. E. 1981, *ApJ*, 249, 462
- Pancoast, A., Brewer, B. J., Treu, T., et al. 2014, *MNRAS*, 445, 3073
- Panda, S. 2021a, in *XIX Serbian Astronomical Conference*, Vol. 100, 333–338
- Panda, S. 2021b, *A&A*, 650, A154
- Panda, S., Martínez-Aldama, M. L., Marinello, M., et al. 2020, *ApJ*, 902, 76
- Parker, M. L., Komossa, S., Kollatschny, W., et al. 2016, *MNRAS*, 461, 1927
- Parker, M. L., Schartel, N., Grupe, D., et al. 2019, *MNRAS*, 483, L88
- Pastoriza, M. & Gerola, H. 1970, *Astrophys. Lett.*, 6, 155
- Penston, M. V. & Perez, E. 1984, *MNRAS*, 211, 33P
- Persson, S. E. 1988a, *ApJ*, 330, 751
- Persson, S. E. 1988b, *PASP*, 100, 710
- Popović, L. Č., Shapovalova, A. I., Ilić, D., et al. 2014, *A&A*, 572, A66
- Pringle, J. E. 1981, *ARA&A*, 19, 137
- Ramolla, M., Haas, M., Westhues, C., et al. 2018, *A&A*, 620, A137
- Ricci, T. V. & Steiner, J. E. 2019, *MNRAS*, 486, 1138
- Richter, O. G. & Sancisi, R. 1994, *A&A*, 290, L9
- Rodríguez-Ardila, A., Viegas, S. M., Pastoriza, M. G., & Prato, L. 2002a, *ApJ*, 565, 140
- Rodríguez-Ardila, A., Viegas, S. M., Pastoriza, M. G., Prato, L., & Donzelli, C. J. 2002b, *ApJ*, 572, 94

- Roming, P. W. A., Kennedy, T. E., Mason, K. O., et al. 2005, *Space Sci. Rev.*, 120, 95
- Ross, N. P., Ford, K. E. S., Graham, M., et al. 2018, *MNRAS*, 480, 4468
- Runnoe, J. C., Cales, S., Ruan, J. J., et al. 2016, *MNRAS*, 455, 1691
- Schimoia, J. S., Storch-Bergmann, T., Grupe, D., et al. 2015, *ApJ*, 800, 63
- Schlafly, E. F. & Finkbeiner, D. P. 2011, *ApJ*, 737, 103
- Schulz, H., Muecke, A., Boer, B., Dresen, M., & Schmidt-Kaler, T. 1995, *A&AS*, 109, 523
- Shappee, B. J., Prieto, J. L., Grupe, D., et al. 2014, *ApJ*, 788, 48
- Shetty, S. & Cappellari, M. 2015, *MNRAS*, 454, 1332
- Shobbrook, R. R. 1966, *MNRAS*, 131, 293
- Short, P., Nicholl, M., Lawrence, A., et al. 2020, *MNRAS*, 498, 4119
- Smajić, S., Moser, L., Eckart, A., et al. 2015, *A&A*, 583, A104
- Śniegowska, M., Czerny, B., Bon, E., & Bon, N. 2020, *A&A*, 641, A167
- Śniegowska, M., Grzędzielski, M., Czerny, B., & Janiuk, A. 2023, *A&A*, 672, A19
- Stern, D., McKernan, B., Graham, M. J., et al. 2018, *ApJ*, 864, 27
- Storch-Bergmann, T., Eracleous, M., Teresa Ruiz, M., et al. 1997, *ApJ*, 489, 87
- Storch-Bergmann, T., Nemmen da Silva, R., Eracleous, M., et al. 2003, *ApJ*, 598, 956
- Strateva, I. V., Strauss, M. A., Hao, L., et al. 2003, *AJ*, 126, 1720
- Sulentic, J. W., Marziani, P., Zamanov, R., et al. 2002, *ApJ*, 566, L71
- Trakhtenbrot, B., Arcavi, I., MacLeod, C. L., et al. 2019a, *ApJ*, 883, 94
- Trakhtenbrot, B., Arcavi, I., Ricci, C., et al. 2019b, *Nature Astronomy*, 3, 242
- Ulrich, M.-H., Maraschi, L., & Urry, C. M. 1997, *ARA&A*, 35, 445
- Valdes, F., Gupta, R., Rose, J. A., Singh, H. P., & Bell, D. J. 2004, *ApJS*, 152, 251
- Veilleux, S. & Zheng, W. 1991, *ApJ*, 377, 89
- Véron, P., Gonçalves, A. C., & Véron-Cetty, M. P. 2002, *A&A*, 384, 826
- Véron-Cetty, M. P., Véron, P., & Gonçalves, A. C. 2001, *A&A*, 372, 730
- Vestergaard, M. & Peterson, B. M. 2006, *ApJ*, 641, 689
- Wanders, I. 1995, *A&A*, 296, 332
- Wang, J.-M. & Bon, E. 2020, *A&A*, 643, L9
- Wang, J.-M., Du, P., Songsheng, Y.-Y., & Li, Y.-R. 2022, *A&A*, 666, A86
- Weilbacher, P. M., Streicher, O., Urrutia, T., et al. 2012, in *Society of Photo-Optical Instrumentation Engineers (SPIE) Conference Series*, Vol. 8451, *Software and Cyberinfrastructure for Astronomy II*, ed. N. M. Radziwill & G. Chiozzi, 84510B
- Weilbacher, P. M., Streicher, O., Urrutia, T., et al. 2014, in *Astronomical Society of the Pacific Conference Series*, Vol. 485, *Astronomical Data Analysis Software and Systems XXIII*, ed. N. Manset & P. Forshay, 451
- Wevers, T., Nicholl, M., Guolo, M., et al. 2022, *A&A*, 666, A6
- Weymann, R. J., Morris, S. L., Foltz, C. B., & Hewett, P. C. 1991, *ApJ*, 373, 23
- Wilkins, D. R. & Fabian, A. C. 2012, *MNRAS*, 424, 1284
- Williams, P. R., Pancoast, A., Treu, T., et al. 2018, *ApJ*, 866, 75
- Winkler, H. 1992, *MNRAS*, 257, 677
- Woo, J.-H. & Urry, C. M. 2002, *ApJ*, 579, 530
- Wright, E. L. 2006, *PASP*, 118, 1711
- Xu, D. W., Komossa, S., Grupe, D., et al. 2024, *Universe*, 10, 61
- Zabludoff, A., Arcavi, I., LaMassa, S., et al. 2021, *Space Sci. Rev.*, 217, 54
- Zetzl, M., Kollatschny, W., Ochmann, M. W., et al. 2018, *A&A*, 618, A83